Inorg. Chem. **2007**, *46*, 8924–8938

Inorganic Chemistry
Article

Tuning of Magnetic Properties of Polynuclear Lanthanide(III)–Octacyanotungstate(V) Systems: Determination of Ligand-Field Parameters and Exchange Interaction

Paweł Przychodzeń,[†] Robert Pełka,*[,‡] Krzysztof Lewiński,[†] Justyna Supel,[†] Michał Rams,[§] Krzysztof Tomala,[§] and Barbara Sieklucka*[,†]

Faculty of Chemistry, Jagiellonian University, Ingardena 3, 30-060 Kraków, Poland, H. Niewodniczański Institute of Nuclear Physics PAN, Radzikowskiego 152, 31-342 Kraków, Poland, and M. Smoluchowski Institute of Physics, Jagiellonian University, Reymonta 4, 30-059 Kraków, Poland

Received April 26, 2007

The self-assembly reaction between trivalent lanthanide ions, 2,2′:6′,2′′-terpyridine (terpy) ligand, and octacyanotungstate(V) leads to the formation of two series of isomorphous cyano-bridged compounds: (i) one-dimensional (1-D) chains $[Ln(terpy)(DMF)_4][W(CN)_8]\cdot 6H_2O\cdot C_2H_5OH$ (Ln = Ce–Dy) and (ii) dinuclear molecules $[Ln(terpy)(DMF)_2(H_2O)_2][W(CN)_8]\cdot 3H_2O$ (Ln = Ho, Er, Yb) and the ionic $[Tm^{III}(terpy)(DMF)_2(H_2O)_3][W^V(CN)_8]\cdot 4H_2O\cdot DMF$ (DMF = *N*,*N*-dimethylformamide) system. The crystal structures of 1-D chains consist of alternating $\{[W(CN)_8]\}$ and $\{[Ln(terpy)]\}$ building blocks. The neighboring chains are weakly linked through the π–π stacking interactions of the aromatic rings, leading to two-dimensional supramolecular layers. The dinuclear species are weakly linked through the hydrogen bonds between H_2O molecules and terminal cyano ligands resulting in a columnlike arrangement of dimers. Taking into account the ligand-field splitting and the exchange interaction, we have estimated the magnetic couplings between the Ln^{III} and W^V centers in a series of polycrystalline 1-D chains and in dimeric systems. The corresponding exchange constants have been shown to change the sign along the series of chains. The coupling is antiferromagnetic for **1** ($J = -0.24$ cm^{-1}) and **2** ($J = -0.07$ cm^{-1}), whereas **3** ($J = +0.47$ cm^{-1}), **7** ($J = +0.28$ cm^{-1}), and **8** ($J = +0.23$ cm^{-1}) have ferromagnetic character. In the case of dimeric systems, the coupling constants seem to be independent of the lanthanide center. The splitting structures of the ground-state multiplets of the Ln^{III} centers have been shown to explain the temperature dependences of the magnetic susceptibilities.

Introduction

Homo- and heterometallic coordination networks based on lanthanide centers offer attractive properties in terms of their material properties and potential applications in data storage, quantum computing, or nonlinear optics.[1] Discrete polynuclear d−f electron systems are of significant interest from the viewpoint of single-molecule-magnet construction.[2] Because of both large-spin and considerable single ion anisotropy provided by lanthanide centers, the rational design of f−d cyano-bridged architectures tuned by the lanthanide center attracts considerable attention in the field of functional magnetic materials. The exploration of cyano-bridged 4f−3d systems resulted in a wide variety of coordination networks from ionic compounds[3] and discrete molecules,[4] through one-dimensional (1-D) chains[4c,5] and two-dimen-

---

* To whom correspondence should be addressed. E-mail: robert.pelka@ifj.edu.pl (R.P.), siekluck@chemia.uj.edu.pl (B.S.). Phone: +48-12-662-82-63 (R.P.), +48-12-633-20-36 (B.S.).

[†] Faculty of Chemistry, Jagiellonian University.

[‡] H. Niewodnicza’nski Institute of Nuclear Physics PAN.

[§] M. Smoluchowski Institute of Physics, Jagiellonian University.

(1) (a) Bünzli, J.-C. G.; Piguet, C. *Chem. Rev.* **2002**, *102*, 1897. (b) Shi, J.-M.; Xu, W.; Liu, Q.-Y.; Liu, F.-L.; Huang, Z.-L.; Lei, H.; Yu, W.-T.; Fang, Q. *Chem. Commun.* **2002**, 756. (c) Sénéchal, K.; Toupet, L.; Ledoux, I.; Zyss, J.; Le Bozec, H.; Maury, O. *Chem. Commun.* **2004**, 2180.

(2) (a) Osa, S.; Kido, T.; Matsumoto, N.; Re, N.; Pochaba, A.; Mroziński, J. *J. Am. Chem. Soc.* **2004**, *126*, 420. (b) Zaleski, C. M.; Depperman, E. C.; Kampf, J. W.; Kirk, M. L.; Pecoraro, V. L. *Angew. Chem., Int. Ed.* **2004**, *43*, 3912. (c) Mishra, A.; Wernsdorfer, W.; Abboud, K. A.; Christou, G. *J. Am. Chem. Soc.* **2004**, *126*, 15648. (d) Mishra, A.; Wernsdorfer, W.; Parsons, S.; Christou, G.; Brechin, E. K. *Chem. Commun.* **2005**, 2086. (e) Ferbinteanu, M.; Kajiwara, T.; Choi, K.-Y.; Nojiri, H.; Nakamoto, A.; Kojima, N.; Cimpoesu, F.; Fujimura, Y.; Takaishi, S.; Yamashita, M. *J. Am. Chem. Soc.* **2006**, *128*, 9008. (f) Mori, F.; Nyui, T.; Ishida, T.; Nogami, T.; Choi, K.-Y.; Nojiri, H. *J. Am. Chem. Soc.* **2006**, *128*, 1440.

10.1021/ic700795q CCC: $37.00

sional (2-D) layers,[4i,5c,i,6] to three-dimensional (3-D) Prussian Blue analogues.[7] When lanthanide−octacyanometalate-based supramolecular magnetic materials are focused on, only three 4f−5d systems have been reported: (i) 2-D ferromagnetic $[Sm^{III}(H_2O)_5][W^{V}(CN)_8]$,[8a] (ii) 1-D antiferromagnetic $[Gd^{III}(DMF)_6][W^{V}(CN)_8]$ (DMF = *N*,*N*-dimethylformamide),[8b] and (iii) 3-D paramagnetic $[Ln(mpca)_2(H_2O)(MeOH)][Ln(H_2O)_6][W(CN)_8]\cdot xH_2O$ (Ln = Eu, Nd).[8c]

The reported networks have been prepared using the building-block approach, in which lanthanide cations are linked by polycyanometalate linkers. The coordination properties of lanthanide centers are difficult to control because of their lability, and in the absence of design strategies for 4f−d networks, it will be challenging to synthesize materials with specific structures and therefore magnetic properties. According to the two isomorphous $[Gd^{III}(terpy)(DMF)_4][W^{V}(CN)_8]\cdot 6H_2O\cdot C_2H_5OH$ and $[Sm^{III}(terpy)(DMF)_4][W^{V}(CN)_8]\cdot 6H_2O\cdot C_2H_5OH$ 1-D chains recently reported by us,[9] here we describe the lanthanide-tuned structural and magnetic characterization of magnetic materials based on the use of 2,2′:6′,2″-terpyridine (terpy) as a blocking ligand at the Ln^{III} center (Ln = paramagnetic lanthanide(III) ions except Pm) and octacyanotungstate(V)-mediating magnetic interaction.

Generally, the magnetic properties of lanthanide-based supramolecular systems were used to be considered similarly to those of isolated ions. However, the magnetic susceptibility is determined by thermal population of sublevels in the ground-state multiplet in the ligand field (LF). This work is focused on studying the nature of magnetic exchange in 1-D chains formed by the early lanthanides of the general formula $[Ln^{III}(terpy)(DMF)_4][W^{V}(CN)_8]\cdot 6H_2O\cdot C_2H_5OH$ ([CeW] (**$1\cdot C_2H_5OH$**), [PrW] (**$2\cdot C_2H_5OH$**), [NdW] (**$3\cdot C_2H_5OH$**), [SmW] (**$4\cdot C_2H_5OH$**), [EuW] (**$5\cdot C_2H_5OH$**), [GdW] (**$6\cdot C_2H_5OH$**), [TbW] (**$7\cdot C_2H_5OH$**), and [DyW] (**$8\cdot C_2H_5OH$**)). Furthermore, we present crystal structures and magnetic analysis for three dimeric systems, $[Ln^{III}(terpy)(DMF)_2(H_2O)_2][W^{V}(CN)_8]\cdot 3H_2O$ ([HoW] (**9**), [ErW] (**10**), and [YbW] (**11**)), formed by the late lanthanides. Finally, we discuss an exceptional behavior of the Tm^{III} precursor, which forms the $[Tm^{III}(terpy)(DMF)_2(H_2O)_3][W^{V}(CN)_8]\cdot 4H_2O\cdot DMF$ ([TmW] (**12**)) ionic compound. The determination of the electronic structure of isolated Ln^{III} centers and $Ln^{III}-W^{V}$ systems, calculations of LF parameters, and exchange coupling constants for the 4f−5d electron complexes was based on a procedure developed by Ishikawa et al., originally applied for mono- and dinuclear homometallic lanthanide-based compounds.[10]

Experimental Section

General Procedures and Materials. All chemicals and solvents were of analytical grade. $Cs_3[W(CN)_8]\cdot 2H_2O$ was prepared according to the literature.[11] The syntheses of all $Ln^{III}-W^{V}$ assemblies were performed in the dark and at room temperature because of the photosensitivity of octacyanotungstate(V) ions.

Preparation of $[Ce^{III}(terpy)(DMF)_4][W^{V}(CN)_8]\cdot 6H_2O$ (1). To a solution of $Ce(NO_3)_3\cdot 6H_2O$ (0.86 mmol, 0.37 g) and $Cs_3[W^{V}(CN)_8]\cdot 2H_2O$ (0.86 mmol, 0.71 g) in water (10 mL) was added a solution of terpy (0.86 mmol, 0.20 g) in ethanol (10 mL). The yellow precipitate was dissolved using ca. 12 mL of DMF. The resulting solution was left in an open beaker for 3 days. The green crystals of **$1\cdot C_2H_5OH$** were collected by suction filtration, washed with ethanol, and air-dried to give the green polycrystalline solid of **1**. Yield: 250 mg, 25%. Anal. Calcd for $C_{35}H_{51}N_{15}O_{10}CeW$ (**1**): C, 36.06; H, 4.41; N, 18.02. Found: C, 35.82; H, 4.40; N, 17.91. IR (KBr): ν(CN) 2147sh, 2157m, 2170m cm^{-1}.

Preparation of $[Pr^{III}(terpy)(DMF)_4][W^{V}(CN)_8]\cdot 6H_2O$ (2). To a solution of $Pr(NO_3)_3\cdot 6H_2O$ (0.86 mmol, 0.37 g) and $Cs_3[W^{V}(CN)_8]\cdot 2H_2O$ (0.86 mmol, 0.71 g) in water (10 mL) was added a solution of terpy (0.86 mmol, 0.20 g) in ethanol (10 mL). The yellow precipitate was dissolved using ca. 12 mL of DMF. The resulting solution was left in an open beaker for 2 days. The yellow crystals of **$2\cdot C_2H_5OH$** were collected by suction filtration, washed

---

(3) Koner, R.; Nayak, M.; Ferguson, G.; Low, J. N.; Glidewell, C.; Misra, P.; Mohanta, S. *CrystEngComm* **2005**, *7*, 129.

(4) (a) Kautz, J. A.; Mullica, D. F.; Cunningham, B. P.; Combs, R. A.; Farmer, J. M. *J. Mol. Struct.* **2000**, *523*, 175. (b) Combs, R. A.; Farmer, J. M.; Kautz, J. A. *Acta Crystallogr.* **2000**, *C56*, 1420. (c) Kou, H.-Z.; Gao, S.; Li, C.-H.; Liao, D.-Z.; Zhou, B.-C.; Wang, R.-J.; Li, Y. *Inorg. Chem.* **2002**, *41*, 4756. (d) Li, G.; Akitsu, T.; Sato, O.; Einaga, Y. *J. Am. Chem. Soc.* **2003**, *125*, 12396. (e) Li, G.; Sato, O.; Akitsu, T.; Einaga, Y. *J. Solid State Chem.* **2004**, *177*, 3835. (f) Li, G.; Akitsu, T.; Sato, O.; Einaga, Y. *J. Coord. Chem.* **2004**, *57*, 189. (g) Yan, B.; Song, Y. *J. Coord. Chem.* **2004**, *57*, 49. (h) Figuerola, A.; Ribas, J.; Llunell, M.; Casanova, D.; Maestro, M.; Alvarez, S.; Diaz, C. *Inorg. Chem.* **2005**, *44*, 6939. (i) Chen, W.-T.; Guo, G.-C.; Wang, M.-S.; Xu, G.; Cai, L.-Z.; Akitsu, T.; Akita-Tanaka, M.; Matsushita, A.; Huang, J.-S. *Inorg. Chem.* **2007**, *46*, 2105.

(5) (a) Yan, B.; Chen, Z.; Wang, S.; Gao, S. *Chem. Lett.* **2001**, 350. (b) Gao, S.; Su, G.; Yi, T.; Ma, B. Q. *Phys. Rev. B* **2001**, *63*, 054431. (c) Kou, H.-Z.; Gao, S.; Jin, X. *Inorg. Chem.* **2001**, *40*, 6295. (d) Tanase, S.; Andruh, M.; Müller, A.; Schmidtmann, M.; Mathonière, C.; Rombaut, G. *Chem. Commun.* **2001**, 1084. (e) Figuerola, A.; Diaz, C.; El Fallah, M. S.; Ribas, J.; Maestro, M.; Mahia, J. *Chem. Commun.* **2001**, 1204. (f) Kou, H.-Z.; Zhou, B. C.; Wang, R.-J. *Inorg. Chem.* **2003**, *42*, 7658. (g) Gheorghe, R.; Andruh, M.; Costes, J.-P.; Donnadieu, B. *Chem. Commun.* **2003**, 2778. (h) Figuerola, A.; Diaz, C.; Ribas, J.; Tangoulis, V.; Sangregorio, C.; Gatteschi, D.; Maestro, M.; Mahia, J. *Inorg. Chem.* **2003**, *42*, 5274. (i) Liu, S.; Plecnik, C. E.; Meyers, E. A.; Shore, S. G. *Inorg. Chem.* **2005**, *44*, 282. (j) Figuerola, A.; Ribas, M.; Casanova, D.; Maestro, M.; Alvarez, S.; Diaz, C. *Inorg. Chem.* **2005**, *44*, 6949. (k) Koner, R.; Drew, M. G. B.; Figuerola, A.; Diaz, C.; Mohanta, S. *Inorg. Chim. Acta* **2005**, *358*, 3041. (l) Ge, C.; Kou, H.-Z.; Ni, Z.-H.; Jiang, Y.-B.; Zhang, L.-F.; Cui, A.-L.; Sato, O. *Chem. Lett.* **2005**, *34*, 1280. (m) Estrader, M.; Ribas, J.; Tangoulis, V.; Solans, X.; Font-Bardia, M.; Maestro, M.; Diaz, C. *Inorg. Chem.* **2006**, *45*, 8239. (n) Gheorghe, R.; Cucos, P.; Andruh, M.; Costes, J.-P.; Donnadieu, B.; Shova, S. *Chem.−Eur. J.* **2006**, *12*, 187.

(6) (a) Ma, B.-Q.; Gao, S.; Su, G.; Xu, G.-X. *Angew. Chem., Int. Ed.* **2001**, *40*, 434. (b) Kou, H.-Z.; Gao, S.; Sun, B.-W.; Zhang, J. *Chem. Mater.* **2001**, *13*, 1431. (c) Kou, H.-Z.; Zhou, B. C.; Gao, S.; Wang, R.-J. *Angew. Chem., Int. Ed.* **2003**, *42*, 3288. (d) Yeung, W.-F.; Lau, T.-C.; Wang, X.-Y.; Gao, S.; Szeto, L.; Wong, W.-T. *Inorg. Chem.* **2006**, *45*, 6756. (e) Zhang, Y.-Z.; Duan, G.-P.; Sato, O.; Gao, S. *J. Mater. Chem.* **2006**, *16*, 2625.

(7) (a) Sun, H.-L.; Shi, H.; Zhao, F.; Qi, L.; Gao, S. *Chem. Commun.* **2005**, 4339. (b) Artemkina, S. B.; Naumov, N. G.; Virovets, A. V.; Fedorov, V. E. *Eur. J. Inorg. Chem.* **2005**, 142.

(8) (a) Hozumi, T.; Ohkoshi, S.-I.; Arimoto, Y.; Seino, H.; Mizobe, Y.; Hashimoto, K. *J. Phys. Chem. B* **2003**, *107*, 11571. (b) Ikeda, S.; Hozumi, T.; Hashimoto, K. *Dalton Trans.* **2005**, 2120. (c) Tanase, S.; Prins, F.; Smits, J. M. M.; de Gelser, R. *CrystEngComm* **2006**, *8*, 863.

(9) Przychodzeń, P.; Lewiński, K.; Pełka, R.; Bałanda, M.; Tomala, K.; Sieklucka, B. *Dalton Trans.* **2006**, 625.

(10) (a) Ishikawa, N.; Iino, T.; Kaizu, Y. *J. Phys. Chem. A* **2002**, *106*, 9543. (b) Ishikawa, N.; Iino, T.; Kaizu, Y. *J. Am. Chem. Soc.* **2002**, *124*, 11440. (c) Ishikawa, N.; Sugita, M.; Okubo, T.; Tanaka, N.; Iino, T.; Kaizu, Y. *Inorg. Chem.* **2003**, *42*, 2440. (d) Ishikawa, N.; Sugita, M.; Wernsdorfer, W. *J. Am. Chem. Soc.* **2005**, *127*, 3650. (e) Ishikawa, N.; Sugita, M.; Wernsdorfer, W. *Angew. Chem., Int. Ed.* **2005**, *44*, 2.

(11) Leipoldt, J. G.; Bok, L. C. D.; Cilliers, P. J. *Z. Anorg. Allg. Chem.* **1974**, *409*, 343.

with ethanol, and air-dried to give the yellow polycrystalline solid of **2**. Yield: 599 mg, 60%. Anal. Calcd for $C_{35}H_{51}N_{15}O_{10}PrW$ (**2**): C, 36.03; H, 4.41; N, 18.01. Found: C, 36.04; H, 4.45; N, 18.06. IR (KBr): ν(CN) 2148sh, 2158m, 2169sh cm^{-1}.

Preparation of [Nd^{III}(terpy)(DMF)$_4$][W^V(CN)$_8$]·6H$_2$O (3). To a solution of $Nd(NO_3)_3·6H_2O$ (0.86 mmol, 0.38 g) and $Cs_3[W^V(CN)_8]·2H_2O$ (0.86 mmol, 0.71 g) in water (10 mL) was added a solution of terpy (0.86 mmol, 0.20 g) in ethanol (10 mL). The yellow precipitate was dissolved using ca. 12 mL of DMF. The resulting solution was left in an open beaker for 2 days. The yellow crystals of **3·C$_2$H$_5$OH** were collected by suction filtration, washed with ethanol, and air-dried to give the yellow polycrystalline solid of **3**. Yield: 692 mg, 69%. Anal. Calcd for $C_{35}H_{51}N_{15}O_{10}NdW$ (**3**): C, 35.93; H, 4.39; N, 17.96. Found: C, 36.31; H, 4.43; N, 17.89. IR (KBr): ν(CN) 2149m, 2161m, 2172m cm^{-1}.

Preparation of [Sm^{III}(terpy)(DMF)$_4$][W^V(CN)$_8$]·6H$_2$O (4). To a solution of $Sm(NO_3)_3·6H_2O$ (0.43 mmol, 0.19 g) and $Cs_3[W^V(CN)_8]·2H_2O$ (0.43 mmol, 0.35 g) in water (10 mL) was added a solution of terpy (0.43 mmol, 0.10 g) in ethanol (10 mL). The yellow precipitate was dissolved using ca. 12 mL of DMF. The resulting solution was left in an open beaker for 10 days. The yellow crystals of **4·C$_2$H$_5$OH** were collected by suction filtration, washed with ethanol, and air-dried to give the yellow polycrystalline solid of **4**. Yield: 145 mg, 29%. Anal. Calcd for $C_{35}H_{51}N_{15}O_{10}SmW$ (**4**): C, 35.74; H, 4.37; N, 17.86. Found: C, 35.72; H, 4.05; N, 17.61. IR (KBr): ν(CN) 2148m, 2165m, 2171sh cm^{-1}.

Preparation of [Eu^{III}(terpy)(DMF)$_4$][W^V(CN)$_8$]·6H$_2$O (5). To a solution of $Eu(NO_3)_3·5H_2O$ (0.86 mmol, 0.37 g) and $Cs_3[W^V(CN)_8]·2H_2O$ (0.86 mmol, 0.71 g) in water (10 mL) was added a solution of terpy (0.86 mmol, 0.20 g) in ethanol (10 mL). The yellow precipitate was dissolved using ca. 12 mL of DMF. The resulting solution was left in an open beaker for 2 days. The yellow crystals of **5·C$_2$H$_5$OH** were collected by suction filtration, washed with ethanol, and air-dried to give the yellow polycrystalline solid of **5**. Yield: 604 mg, 60%. Anal. Calcd for $C_{35}H_{51}N_{15}O_{10}EuW$ (**5**): C, 35.70; H, 4.36; N, 17.84. Found: C, 35.92; H, 4.25; N, 17.67. IR (KBr): ν(CN) 2147m, 2167m cm^{-1}.

Preparation of [Gd^{III}(terpy)(DMF)$_4$][W^V(CN)$_8$]·6H$_2$O (6). To a solution of $Gd(NO_3)_3·6H_2O$ (0.43 mmol, 0.19 g) and $Cs_3[W^V(CN)_8]·2H_2O$ (0.43 mmol, 0.35 g) in water (10 mL) was added a solution of terpy (0.43 mmol, 0.10 g) in ethanol (10 mL). The yellow precipitate was dissolved using ca. 12 mL of DMF. The resulting solution was left in an open beaker for 10 days. Then diisopropyl ether was slowly diffused. After 1 day, the yellow crystals of **6·C$_2$H$_5$OH** were collected by suction filtration, washed with ethanol, and air-dried to give the yellow polycrystalline solid of **6**. Yield: 220 mg, 44%. Anal. Calcd for $C_{35}H_{51}N_{15}O_{10}GdW$ (**6**): C, 35.54; H, 4.35; N, 17.76. Found: C, 35.84; H, 4.05; N, 17.66. IR (KBr): ν(CN) 2147m, 2168m, 2171sh cm^{-1}.

Preparation of [Tb^{III}(terpy)(DMF)$_4$][W^V(CN)$_8$]·6H$_2$O (7). To a solution of $Tb(NO_3)_3·5H_2O$ (0.86 mmol, 0.37 g) and $Cs_3[W^V(CN)_8]·2H_2O$ (0.86 mmol, 0.71 g) in water (10 mL) was added a solution of terpy (0.86 mmol, 0.20 g) in ethanol (10 mL). The yellow precipitate was dissolved using ca. 12 mL of DMF. The resulting solution was left in an open beaker for 3 days. The yellow crystals of **7·C$_2$H$_5$OH** were collected by suction filtration, washed with ethanol, and air-dried to give the yellow polycrystalline solid of **7**. Yield: 202 mg, 20%. Anal. Calcd for $C_{35}H_{51}N_{15}O_{10}TbW$ (**7**): C, 35.49; H, 4.34; N, 17.74. Found: C, 35.61; H, 4.33; N, 17.55. IR (KBr): ν(CN) 2146m, 2169m cm^{-1}.

Preparation of [Dy^{III}(terpy)(DMF)$_4$][W^V(CN)$_8$]·6H$_2$O (8). To a solution of $Dy(NO_3)_3·5H_2O$ (0.86 mmol, 0.38 g) and $Cs_3[W^V(CN)_8]·2H_2O$ (0.86 mmol, 0.71 g) in water (10 mL) was added a solution of terpy (0.86 mmol, 0.20 g) in ethanol (10 mL). The yellow precipitate was dissolved using ca. 12 mL of DMF. The resulting solution was left in an open beaker for 5 days. The yellow crystals of **8·C$_2$H$_5$OH** were collected by suction filtration, washed with ethanol, and air-dried to give the yellow polycrystalline solid of **8**. Yield: 430 mg, 42%. Anal. Calcd for $C_{35}H_{51}N_{15}O_{10}DyW$ (**8**): C, 35.38; H, 4.33; N, 17.68. Found: C, 35.20; H, 4.12; N, 17.60. IR (KBr): ν(CN) 2147m, 2169m, 2172sh cm^{-1}.

Preparation of [Ho^{III}(terpy)(DMF)$_2$(H$_2$O)$_2$][W^V(CN)$_8$]·3H$_2$O (9). To a solution of $Ho(NO_3)_3·5H_2O$ (0.86 mmol, 0.38 g) and $Cs_3[W^V(CN)_8]·2H_2O$ (0.86 mmol, 0.71 g) in water (10 mL) was added a solution of terpy (0.86 mmol, 0.20 g) in ethanol (10 mL). Then, 10 mL of DMF was added. The resulting solution was left in an open beaker for 3 days. The yellow crystals of **9** were collected by suction filtration, washed with ethanol, and air-dried. Yield: 380 mg, 43%. Anal. Calcd for $C_{29}H_{35}N_{13}O_7HoW$ (**9**): C, 33.93; H, 3.44; N, 17.74. Found: C, 34.04; H, 3.41; N, 17.73. IR (KBr): ν(CN) 2146m, 2176m cm^{-1}.

Preparation of [Er^{III}(terpy)(DMF)$_2$(H$_2$O)$_2$][W^V(CN)$_8$]·3H$_2$O (10). To a solution of $Er(NO_3)_3·5H_2O$ (0.86 mmol, 0.38 g) and $Cs_3[W^V(CN)_8]·2H_2O$ (0.86 mmol, 0.71 g) in water (10 mL) was added a solution of terpy (0.86 mmol, 0.20 g) in ethanol (10 mL). The yellow precipitate was dissolved using ca. 12 mL of DMF. The resulting solution was left in an open beaker for 3 days. The yellow crystals of **10** were collected by suction filtration, washed with ethanol, and air-dried. Yield: 220 mg, 25%. Anal. Calcd for $C_{29}H_{35}N_{13}O_7ErW$ (**10**): C, 33.86; H, 3.43; N, 17.70. Found: C, 34.06; H, 3.79; N, 17.50. IR (KBr): ν(CN) 2147m, 2177m cm^{-1}.

Preparation of [Yb^{III}(terpy)(DMF)$_2$(H$_2$O)$_2$][W^V(CN)$_8$]·3H$_2$O (11). To a solution of $Yb(NO_3)_3·5H_2O$ (0.86 mmol, 0.39 g) and $Cs_3[W^V(CN)_8]·2H_2O$ (0.86 mmol, 0.71 g) in water (10 mL) was added a solution of terpy (0.86 mmol, 0.20 g) in DMF (10 mL). The resulting solution was left in an open beaker for 3 days. Then, 10 mL of ethanol was added. The yellow crystals of **11** were collected by suction filtration, washed with ethanol, and air-dried. Yield: 460 mg, 52%. Anal. Calcd for $C_{29}H_{35}N_{13}O_7YbW$ (**11**): C, 33.67; H, 3.41; N, 17.60. Found: C, 33.47; H, 3.28; N, 17.48. IR (KBr): ν(CN) 2148m, 2178m cm^{-1}.

Preparation of [Tm^{III}(terpy)(DMF)$_2$(H$_2$O)$_3$][W^V(CN)$_8$]·4H$_2$O·DMF (12). To a solution of $Tm(NO_3)_3·5H_2O$ (0.86 mmol, 0.38 g) and $Cs_3[W^V(CN)_8]·2H_2O$ (0.86 mmol, 0.71 g) in water (10 mL) was added a solution of terpy (0.86 mmol, 0.20 g) in ethanol (10 mL). Then, 12 mL of DMF was added. The resulting solution was left in an open beaker for 3 days. The yellow crystals of **12** were collected by suction filtration, washed with ethanol, and air-dried. Yield: 25 mg, 2.6%. Anal. Calcd for $C_{32}H_{46}N_{14}O_{10}TmW$ (**12**): C, 33.73; H, 4.07; N, 17.21. Found: C, 33.58; H, 3.77; N, 17.43. IR (KBr): ν(CN) 2137m, 2147m, 2159m cm^{-1}.

Physical Measurements. Elemental analyses were performed on a EuroEA EuroVector elemental analyzer. IR spectra were measured between 4000 and 400 cm^{-1} on a Bruker EQUINOX 55 spectrometer in KBr disks for powder samples of **1**−**12**. Magnetic susceptibility measurements were performed upon cooling in a constant magnetic field of 1 kOe over the temperature range 1.9−300 K using a Quantum Design SQUID magnetometer. Isothermal magnetization curves in the field up to 50 kOe were measured at $T = 2$ K. Magnetic studies have been carried out for powder samples of **1**−**12**. The single-crystal sample of **10** (approximate size 4.7 × 0.8 × 0.6 mm^3) was oriented by the X-ray analysis.

X-ray Data Collection and Structure Determination. Single-crystal X-ray data for **1·C$_2$H$_5$OH**−**8·C$_2$H$_5$OH** and **9**−**12** were collected at 100 K on a Nonius Kappa CCD diffractometer with graphite-monochromated Mo Kα radiation ($\lambda = 0.7107$ Å), except

Table 1. Crystallographic Data for **$1\cdot C_2H_5OH$−$4\cdot C_2H_5OH$**

	$1\cdot C_2H_5OH$	**$2\cdot C_2H_5OH$**	**$3\cdot C_2H_5OH$**	**$4\cdot C_2H_5OH$**
empirical formula	$C_{37}H_{57}N_{15}O_{11}CeW$	$C_{37}H_{57}N_{15}O_{11}PrW$	$C_{37}H_{57}N_{15}O_{11}NdW$	$C_{37}H_{57}N_{15}O_{11}SmW$
fw	1211.95	1212.74	1216.07	1222.18
λ (Å)	0.710 70	0.710 70	0.710 70	0.710 70
cryst syst	monoclinic	monoclinic	monoclinic	monoclinic
space group	$P2_1/n$	$P2_1/n$	$P2_1/n$	$P2_1/n$
a (Å)	14.5980(2)	14.3840(2)	14.3360(2)	14.50900(10)
b (Å)	23.7530(3)	23.4370(2)	23.4180(3)	23.6780(3)
c (Å)	14.8350(2)	14.7350(2)	14.7130(2)	14.74700(10)
β (deg)	90.3980(7)	90.2880(6)	90.4620(6)	90.8760(7)
V (Å^3)	5143.86(12)	4967.37(11)	4939.29(12)	5065.65(8)
Z	4	4	4	4
ρ_{calc} (g cm^{-3})	1.565	1.622	1.635	1.603
μ (mm^{-1})	3.174	3.351	3.435	3.483
T (K)	100(1)	100(1)	100(1)	293(2)
reflns colld	18 302	18 279	19 545	19 058
unique	11 394	10 865	11 185	11 288
obs [$I > 2\sigma(I)$]	8922	9846	9990	9152
R [$I > 2\sigma(I)$]	R1 = 0.0364 wR2 = 0.0795	R1 = 0.0340 wR2 = 0.0789	R1 = 0.0374 wR2 = 0.0843	R1 = 0.0327 wR2 = 0.0764
R (all data)	R1 = 0.0555 wR2 = 0.0878	R1 = 0.0398 wR2 = 0.0815	R1 = 0.0441 wR2 = 0.0866	R1 = 0.0477 wR2 = 0.0842
GOF	1.027	1.158	1.253	1.031

Table 2. Crystallographic Data for **$5\cdot C_2H_5OH$−$8\cdot C_2H_5OH$**

	$5\cdot C_2H_5OH$	**$6\cdot C_2H_5OH$**	**$7\cdot C_2H_5OH$**	**$8\cdot C_2H_5OH$**
empirical formula	$C_{37}H_{57}N_{15}O_{11}EuW$	$C_{37}H_{57}N_{15}O_{11}GdW$	$C_{37}H_{57}N_{15}O_{11}TbW$	$C_{37}H_{57}N_{15}O_{11}DyW$
fw	1223.79	1229.08	1230.75	1234.33
λ (Å)	0.710 70	0.710 70	0.710 70	0.710 70
cryst syst	monoclinic	monoclinic	monoclinic	monoclinic
space group	$P2_1/n$	$P2_1/n$	$P2_1/n$	$P2_1/n$
a (Å)	14.2370(2)	14.48200(10)	14.2070(2)	14.4080(2)
b (Å)	23.4170(3)	23.6880(3)	23.4340(4)	23.7100(3)
C (Å)	14.6690(2)	14.71300(10)	14.6280(2)	14.6670(2)
β (deg)	90.9190(5)	91.1910(10)	91.2790(9)	91.5380(9)
V (Å^3)	4889.84(11)	5046.20(8)	4868.84(13)	5008.64(12)
Z	4	4	4	4
ρ_{calc} (g cm^{-3})	1.662	1.618	1.679	1.637
μ (mm^{-1})	3.690	3.647	3.871	3.842
T (K)	100(1)	293(2)	100(1)	293(2)
reflns colld	19 675	19 832	19 736	19 358
unique	11 074	11 539	10 990	10 963
obsd [$I > 2\sigma(I)$]	10 146	9570	9234	10 029
R [$I > 2\sigma(I)$]	R1 = 0.0352 wR2 = 0.0817	R1 = 0.0319 wR2 = 0.0706	R1 = 0.0345 wR2 = 0.0725	R1 = 0.0291 wR2 = 0.0659
R (all data)	R1 = 0.0401 wR2 = 0.0835	R1 = 0.0451 wR2 = 0.0771	R1 = 0.0468 wR2 = 0.0770	R1 = 0.0337 wR2 = 0.0678
GOF	1.200	1.039	1.041	1.076

$4\cdot C_2H_5OH$, **$6\cdot C_2H_5OH$**, and **$8\cdot C_2H_5OH$**, where X-ray data collection was carried on a single crystal mounted in a glass capillary with a few drops of the mother solution. For cell refinement and data reduction, the Denzo-Scalepack program package was used.[12] The multiscan absorption correction was applied to the data. The structures of **$1\cdot C_2H_5OH$**, **$3\cdot C_2H_5OH$**, **$4\cdot C_2H_5OH$**, and **12** were solved by the heavy-atom method (*SHELXS-97*), except **$6\cdot C_2H_5OH$**, which was solved by direct methods. The structures of **$2\cdot C_2H_5OH$**, **$5\cdot C_2H_5OH$**, **$7\cdot C_2H_5OH$**, **$8\cdot C_2H_5OH$**, and **9**−**11** were solved by direct methods using *SIR92*.[13a] All structures were refined by full-matrix least squares on F^2 using the program *SHELXL-97*.[13b] The N51 DMF molecule was observed as disordered, and two alternative rigid molecules with complementary occupancy factors were used in the refinement. For compounds **$1\cdot C_2H_5OH$−$8\cdot C_2H_5OH$**, **11**, and **12**, N51, N53, and N71 DMF molecules, respectively, were observed as disordered, and two alternative rigid molecules with complementary occupancy factors were used in the refinement. All atoms of these molecules were refined with an isotropic displacement parameter. All non-hydrogen atoms were refined anisotropically. All hydrogen atoms in ordered DMF and terpy molecules were included at idealized positions and refined with isotropic displacement parameters set at 1.5 times that of the bonded atoms. For disordered DMF ligands and H_2O molecules in **$1\cdot C_2H_5OH$−$8\cdot C_2H_5OH$**, hydrogen atoms were not included during the refinement. Complete crystallographic data and collection parameters for **$1\cdot C_2H_5OH$−$8\cdot C_2H_5OH$** and **9**−**12** are listed in Tables 1−3.

Results and Discussion

Structural Description of $1\cdot C_2H_5OH$−$8\cdot C_2H_5OH$. The crystal structures of **$1\cdot C_2H_5OH$−$8\cdot C_2H_5OH$** consist of isomorphous 1-D chains built by alternating W^{V} and Ln^{III} metal centers originating from [Ln(terpy)$(DMF)_4$] (Ln = Ce−Dy) and $[W(CN)_8]$ entities linked through the single cyano bridges (Figure 1). Relevant bond distances and angles are listed in Table 4. The nine-coordinated Ln^{III} centers

---

(12) Otwinowski, Z.; Minor, W. *Methods Enzymol.* **1997**, *276*, 307.

(13) (a) Altomare, A.; Cascarano, G.; Giacovazzo, G.; Guagliardi, A.; Burla, M. C.; Polidori, G.; Camalli, M. *SIR92*—a program for automatic solution of crystal structures by direct methods. *J. Appl. Crystallogr.* **1994**, *27*, 435. (b) Sheldrick, G. M. *SHELX-97: programs for structure analysis*; University of Göttingen: Göttingen, Germany, 1998.

Table 3. Crystallographic Data for **9**−**12**

	9	**10**	**11**	**12**
empirical formula	$C_{29}H_{35}N_{13}O_7HoW$	$C_{29}H_{35}N_{13}O_7ErW$	$C_{29}H_{35}N_{13}O_7YbW$	$C_{32}H_{46}N_{14}O_{10}TmW$
fw	1026.48	1028.81	1034.59	1139.61
λ (Å)	0.710 70	0.710 70	0.710 70	0.710 70
cryst syst	monoclinic	monoclinic	monoclinic	monoclinic
space group	$P2_1$	$P2_1$	$P2_1$	$C2/c$
a (Å)	9.7110(2)	9.7160(2)	9.71800(10)	32.9810(2)
b (Å)	12.2750(3)	12.2480(2)	12.2110(2)	20.23600(10)
c (Å)	15.6390(4)	15.6270(2)	15.6360(2)	26.1510(2)
β (deg)	94.7820(10)	94.8140(10)	94.7630(10)	96.48
V (Å^3)	1857.72(8)	1853.08(5)	1849.06(4)	17341.83(19)
Z	2	2	2	16
ρ_{calc} (g cm^{-3})	1.835	1.844	1.858	1.746
μ (mm^{-1})	5.269	5.411	5.683	4.751
T (K)	100(1)	100(1)	100(1)	100(1)
reflns colld	7291	8086	7907	37 243
unique	7291	8086	7907	19 732
obsd [$I > 2\sigma(I)$]	7053	7895	7775	16 377
R [$I > 2\sigma(I)$]	R1 = 0.0253 wR2 = 0.0561	R1 = 0.0214 wR2 = 0.0478	R1 = 0.0243 wR2 = 0.0593	R1 = 0.0287 wR2 = 0.0584
R (all data)	R1 = 0.0271 wR2 = 0.0570	R1 = 0.0224 wR2 = 0.0482	R1 = 0.0250 wR2 = 0.0597	R1 = 0.0403 wR2 = 0.0621
GOF	1.066	1.064	1.063	1.035

Table 4. Relevant Bond Lengths (Å) and Angles (deg) for Compounds **1·C_2H_5OH−8·C_2H_5OH** with Estimated Standard Deviations in Parentheses

	[CeW]	[PrW]	[NdW]	[SmW]	[EuW]	[GdW]	[TbW]	[DyW]
Ln−N1	2.671(4)	2.621(3)	2.601(4)	2.603(4)	2.561(4)	2.589(4)	2.540(4)	2.542(3)
Ln−N5	2.632(4)	2.590(4)	2.569(4)	2.573(4)	2.533(4)	2.558(4)	2.507(4)	2.520(3)
Ln−N11	2.653(4)	2.626(4)	2.609(4)	2.600(4)	2.573(4)	2.579(3)	2.554(3)	2.554(3)
Ln−N12	2.680(4)	2.642(3)	2.613(4)	2.603(4)	2.580(4)	2.575(4)	2.552(4)	2.566(3)
Ln−N13	2.637(4)	2.617(4)	2.602(4)	2.591(4)	2.573(4)	2.566(4)	2.552(4)	2.569(3)
Ln−O31	2.493(3)	2.471(3)	2.456(3)	2.433(3)	2.411(3)	2.419(3)	2.395(3)	2.415(3)
Ln−O41	2.460(4)	2.452(3)	2.434(4)	2.403(3)	2.402(3)	2.387(3)	2.376(3)	2.398(3)
Ln−O51	2.445(3)	2.437(3)	2.435(3)	2.404(4)	2.394(3)	2.385(3)	2.375(3)	2.392(3)
Ln−O61	2.471(3)	2.457(3)	2.449(4)	2.424(3)	2.407(3)	2.406(3)	2.388(3)	2.407(3)
Ln−N1−C1	169.9(4)	169.8(3)	170.4(4)	171.2(4)	171.0(4)	171.2(4)	171.5(3)	171.6(3)
Ln−N5−C5	168.4(4)	168.5(4)	168.2(4)	169.6(4)	168.2(4)	170.4(4)	169.6(4)	169.8(3)

Table 5. Relevant Hydrogen Bond Lengths (Å) for Compounds **1·C_2H_5OH−8·C_2H_5OH**

D−A	[CeW]	[PrW]	[NdW]	[SmW]	[EuW]	[GdW]	[TbW]	[DyW]
O1−N3	2.989	2.940	2.939	2.968	2.943	2.954	2.948	2.958
O1−N8	2.938	2.916	2.911	2.935	2.921	2.941	2.915	2.957

display frequently adopted tricapped trigonal-prismatic (TTP) geometry composed of one terpy ligand, four DMF molecules, and two nitrogen-bound cyanides. In all compounds, the [$W^V(CN)_8$] moiety has a slightly distorted square-antiprismatic (SAPR) geometry with two bridging and six terminal cyano ligands. The cyanide bridges are exceptionally long and slightly bent [range between 168.2(4)° and 171.6(3)° for Ln−N−C angle] because of the large ionic radii of the Ln^{III} centers. The Ln−N bond lengths vary from 2.671(4) Å for Ln−N1 in [CeW] (**1·C_2H_5OH**) to 2.507(4) Å for Ln−N5 in [TbW] (**7·C_2H_5OH**). Generally, the cyano bridges become shorter and less bent across the series of chains because of the systematic ionic radii contraction. The Ln−ligand donor atom distances are in good agreement with the bond lengths found for [Ln(terpy)] entities in mononuclear complexes.[14] The metric parameters of Ln−NC−W linkages conform to those observed in octacyano- and lanthanide-based systems.[8]

The neighboring {$Ln^{III}W^V$} chains weakly interact through the face-to-face $\pi-\pi$ stacking of the terpy aromatic rings, leading to the 2-D supramolecular folded layer (Figure 2). This results in relatively long intermetallic distances (9.1 and 9.3 Å for Ln···W and Ln···Ln, respectively). The 2-D layers are linked through the hydrogen bonds between H_2O molecules and terminal cyano ligands (Figure 3). The O1−N3 and O1−N8 hydrogen bond lengths are listed in Table 5. The donor−acceptor distances suggest the medium strength of the hydrogen bonds. The DMF ligands at the Ln^{III} centers are not engaged in the hydrogen bonding. The IR spectra measurements performed on powder samples of **1**−**8** reveal ν(CN) bands within the range of 2146−2172 cm^{-1}, consistent with maintenance of the W^V site.

Structural Description of 9−11. The crystal structures of **9**−**11** consist of isomorphous dinuclear molecules built by W^V and Ln^{III} metal centers linked through the single cyano bridge (Figure 4). Relevant bond distances and angles are presented in Table 6. The eight-coordinated Ln^{III} centers

---

(14) (a) Cotton, S. A.; Raithby, P. R. *Inorg. Chem. Commun.* **1999**, *2*, 86. (b) Drew, M. G. B.; Iveson, P. B.; Hudson, M. J.; Liljenzin, J. O.; Spjuth, L.; Cordier, P.-Y.; Enarsson, A.; Hill, C.; Madic, C. *J. Chem. Soc., Dalton Trans.* **2000**, 821. (c) Ahrens, B.; Cotton, S. A.; Feeder, N.; Noy, O. E.; Raithby, P. R.; Teat, S. J. *J. Chem. Soc., Dalton Trans.* **2002**, 2027.

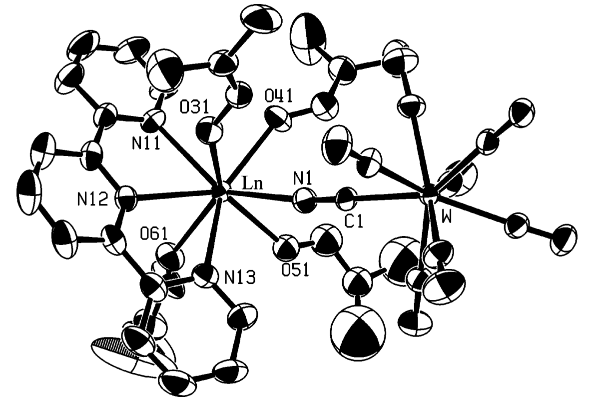

Figure 1. Asymmetric unit of **$1\cdot C_2H_5OH-8\cdot C_2H_5OH$**. The solvent of crystallization has been removed for clarity.

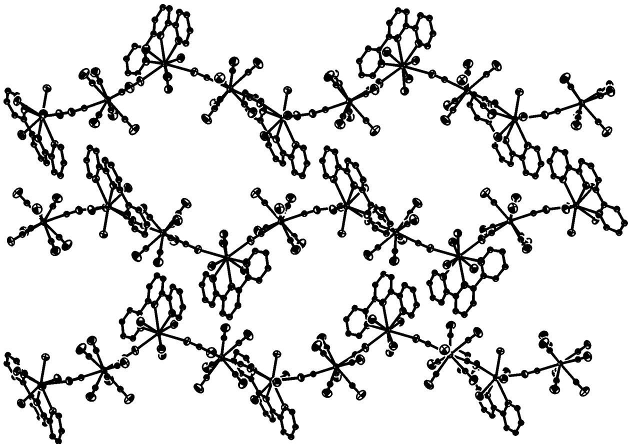

Figure 2. 1-D chains of **$1\cdot C_2H_5OH-8\cdot C_2H_5OH$** forming 2-D supramolecular layers. The solvent of crystallization has been removed for clarity.

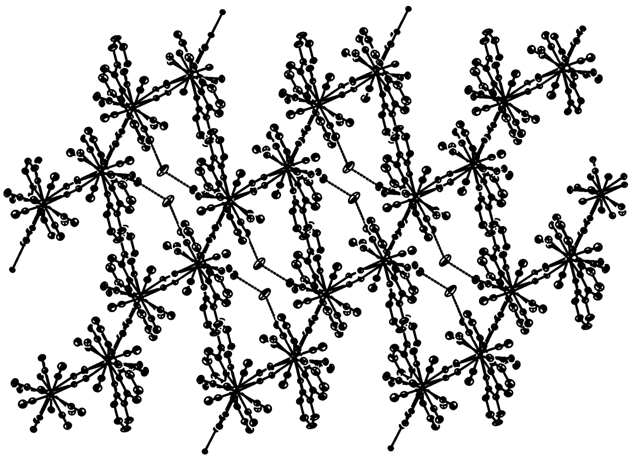

Figure 3. Hydrogen bonds between 2-D supramolecular layers of **$1\cdot C_2H_5OH-8\cdot C_2H_5OH$**.

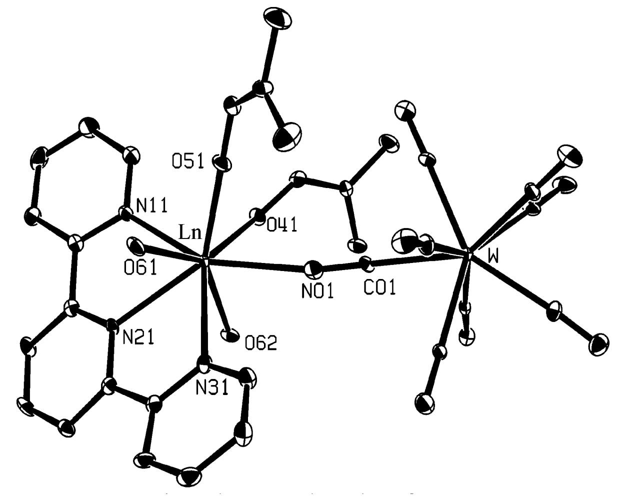

Figure 4. Dinuclear molecule of **9**−**11**.

Table 6. Relevant Bond Lengths (Å) and Angles (deg) for Compounds **9**−**11** with Estimated Standard Deviations in Parentheses

	[HoW]	[ErW]	[YbW]
Ln−N01	2.443(5)	2.432(4)	2.415(4)
Ln−N11	2.448(4)	2.436(3)	2.425(4)
Ln−N21	2.466(4)	2.461(3)	2.440(4)
Ln−N31	2.502(4)	2.504(4)	2.483(4)
Ln−O41	2.323(4)	2.321(3)	2.289(4)
Ln−O51	2.267(4)	2.265(3)	2.244(4)
Ln−O61	2.334(4)	2.310(3)	2.286(4)
Ln−O62	2.346(4)	2.335(3)	2.308(4)
Ln−N01−C01	170.1(4)	169.2(4)	169.1(4)

display SAPR geometry composed of one terpy ligand, two DMF molecules, two H_2O ligands, and one nitrogen-bound cyanide. In all compounds, the $[W^{V}(CN)_8]$ moiety has a SAPR geometry with one bridging and seven terminal cyano ligands. The cyanide bridges are again exceptionally long and slightly bent [range between 169.1(4)° and 170.1(3)° for the Ln−N−C angle] because of the large ionic radii of the Ln^{III} centers. The Ln−N bond lengths vary from 2.443(4) Å for Ln−N01 in [HoW] (**9**) to 2.415(4) Å for Ln−N01 in [YbW] (**11**). The cyano bridge is shorter in the case of $[Yb(terpy)(DMF)_2(H_2O)_2][W(CN)_8]\cdot 3H_2O$ than in $[Ho(terpy)(DMF)_2(H_2O)_2][W(CN)_8]\cdot 3H_2O$ because of the systematic ionic radii contraction. The Ln−ligand donor atom distances are in good agreement with the bond lengths found for [Ln(terpy)] entities in mononuclear complexes.[14] The metric parameters of Ln−NC−W linkages conform to those observed in octacyano- and lanthanide-based systems.[8]

The neighboring $[Ln(terpy)(DMF)_2(H_2O)_2][W^{V}(CN)_8]$ chains are linked through the hydrogen bonds between H_2O molecules and terminal cyano ligands, resulting in a columnlike arrangement of the dimers (Figure 5). The O63−N04, O63−N08, O64−N06, and O64−N07 hydrogen bond lengths are listed in Table 7. The donor−acceptor distances suggest the medium strength of the hydrogen bonds. The DMF ligands at the Ln^{III} centers are not engaged in the hydrogen bonding. The IR spectra measurements performed on powder samples of **9**−**11** reveal ν(CN) bands within the range of 2146−2178 cm^{-1}, consistent with the maintenance of the W^{V} site.

Structural Description of 12. The crystal structure of ionic $[Tm^{III}(terpy)(DMF)_2(H_2O)_3][W^{V}(CN)_8]\cdot 4H_2O\cdot DMF$ consists of $[Tm(terpy)(DMF)_2(H_2O)_3]^{3+}$ cations, $[W(CN)_8]^{3-}$ anionic moieties, and crystallization H_2O and DMF molecules (Figure 6). Relevant bond distances and angles are presented in Table 8. The eight-coordinated Tm^{III} centers display SAPR geometry composed of one terpy ligand, two DMF molecules, and three H_2O ligands. In the $[W^{V}(CN)_8]$ moiety, eight nonbridging cyano ligands are arranged in a SAPR geometry. Molecules of crystallization H_2O and cyano

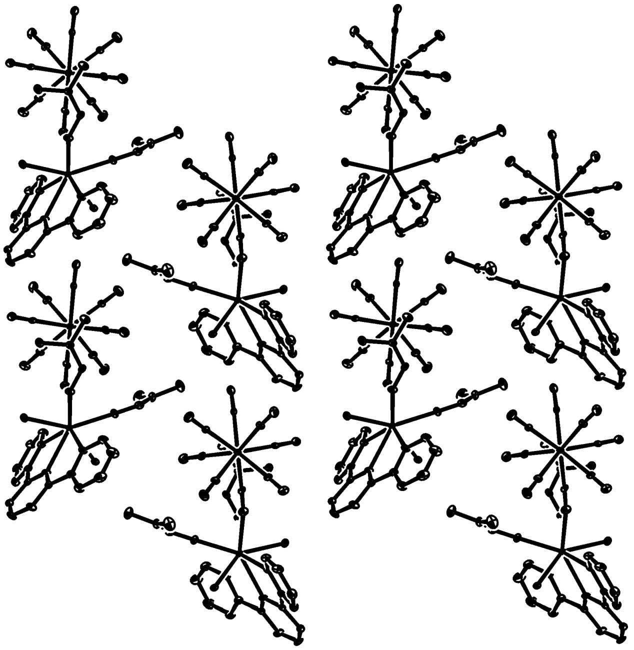

Figure 5. Columnlike arrangement of **9**−**11** dimeric molecules.

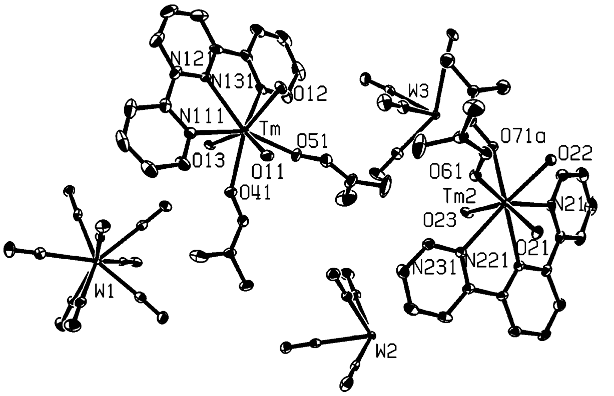

Figure 6. Asymmetric unit of [TmW] (**12**). The solvent of crystallization has been removed for clarity.

Table 7. Relevant Hydrogen Bond Lengths (Å) for Compounds **9**−**11**

D−A	[HoW]	[ErW]	[YbW]
O63−N04	2.906	2.914	2.899
O63−N08	2.817	2.826	2.817
O64−N06	2.864	2.869	2.870
O64−N07	2.856	2.858	2.859

Table 8. Relevant Bond Lengths (Å) for [TmW] (**12**) with Estimated Standard Deviations in Parentheses

Tm−N111	2.460(3)	Tm2−N211	2.468(3)
Tm−N121	2.451(3)	Tm2−N221	2.482(3)
Tm−N131	2.483(3)	Tm2−N231	2.480(3)
Tm−O11	2.336(3)	Tm2−O21	2.288(3)
Tm−O12	2.299(2)	Tm2−O22	2.324(3)
Tm−O13	2.328(3)	Tm2−O23	2.270(3)
Tm−O41	2.304(2)	Tm2−O61	2.295(2)
Tm−O51	2.264(2)	Tm2−O71a	2.302(6)

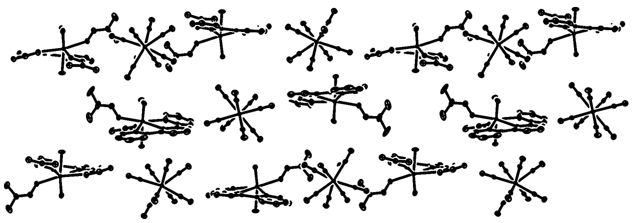

Figure 7. Packing diagram for [TmW] (**12**).

Table 9. Relevant Hydrogen Bond Lengths (Å) for [TmW] (**12**)

D−A		D−A	
O31−N107	2.884	O37−N105	3.089
O31−N303	2.881	O38−N304	2.815
O32−N101	2.842	O11−O32	2.710
O32−N108	3.045	O11−O33	2.698
O33−N108	2.909	O12−O31	2.675
O33−N202	2.851	O12−O37	2.638
O34−N105	2.892	O21−O34	2.639
O34−N201	2.803	O21−O35	2.646
O35−N204	2.964	O22−O36	2.742
O36−N103	2.990	O22−O38	2.631
O36−N302	2.905		

ligands form hydrogen bonds of medium strength, as suggested by donor−acceptor distances (Table 9). The coordinated H_2O molecules are involved in hydrogen bonding with H_2O molecules binding $[W(CN)_8]^{3-}$ anions. This results in an alternating arrangement of $[Tm(terpy)(DMF)_2(H_2O)_3]^{3+}$ and $[W(CN)_8]^{3-}$ in the crystal (Figure 7). The IR spectra measurements performed on a powder sample of **12** reveal three ν(CN) bands at 2137, 2147, and 2159 cm^{-1}, consistent with the maintenance of the W^V site.

Magnetic Properties

General Procedures. According to the procedure of Ishikawa et al. applied originally for mono- and dinuclear homometallic lanthanide-based compounds,[10] we present an approach based solely on the magnetic data that was used to estimate the exchange interaction between the Ln^{III} and W^V centers.

The exchange interaction between the Ln^{III} and W^V centers can be assumed as much weaker than the LF effects and initially neglected. The first step of the procedure (dependent on the coordination number of the Ln^{III} center) consists of tuning of the LF parameters so that the magnetic data are reproduced satisfactorily. Then the simulated data are corrected for the presence of $Ln^{III}-W^V$ coupling. The calculations for 1-D chains are performed for systems containing $N = 5$ $Ln^{III}-W^V$ pairs.

The total angular momentum of the ground state in the trivalent lanthanide ions takes either the minimal value $\mathbf{J} = |\mathbf{L} - \mathbf{S}|$ (for f^1-f^6 configurations) or the maximal value $\mathbf{J} = \mathbf{L} + \mathbf{S}$ (for f^8-f^{13}) in the Russell−Saunders coupling scheme. The simulations were carried out using the $2\mathbf{J} + 1$ sublevels of the ground-state multiplet in each lanthanide system except the Eu^{III} and Sm^{III} complexes, where the energy gap between the ground-state and the first excited-state multiplet is known to be small.[15] As a consequence, the low-lying excited states may become thermally populated. Additionally, coupling through the Zeeman perturbation between substates of different multiplets in the same ground-state term also has to be taken into account. Therefore, these

---

(15) Kahn, O. *Molecular Magnetism*; VCH: New York, 1993; Chapter 3.

cases need a separate treatment from that presented here, i.e., $[Sm^{III}(terpy)(DMF)_4][W^{V}(CN)_8]\cdot 6H_2O$ described previously.[9,16]

The Hamiltonian pertinent to the present systems under an external magnetic field is defined as $H_0 = H_Z + H_{LF}$. The first term accounts for the Zeeman effect:

$$H_Z = \beta(\mathbf{J}\cdot\mathbf{g}_{Ln} + \mathbf{S}\cdot\mathbf{g}_W)\mathbf{H}$$

where β is the Bohr magneton and $\mathbf{H}$ denotes the external magnetic field. The total magnetic moment operator $\mu = \beta(\mathbf{J}\cdot\mathbf{g}_{Ln} + \mathbf{S}\cdot\mathbf{g}_W)$ is used in the corresponding $|\mathbf{J},\mathbf{J}_z\rangle$ representation in its lanthanide part. The S operator denotes the half spin operator of the tungsten center. The $\mathbf{g}_W$ tensor is assumed to be isotropic with its principal values fixed at $\mathbf{g}_W = 2$, whereas the components of $\mathbf{g}_{Ln}$, which we assume to be diagonal, were varied during the fitting procedure. The H_{LF} term corresponds to the LF interaction, which is expressed in the framework of the extended operator equivalent approach.[17−19] The LF part of the isolated-ion Hamiltonian can be expressed as

$$H_{LF} = \sum_{k=2,4,6} \sum_{q=-k}^{+k} B_k^q \mathbf{O}_k^q$$

where the B_k^q coefficients are intended to determine. The $\mathbf{O}_k^q$ matrices are polynomials of the total angular momentum matrices $\mathbf{J}^2$, $\mathbf{J}_z$, $\mathbf{J}_+$, and $\mathbf{J}_-$ (exact definitions are given in the Supporting Information in Table S1). The operator equivalents $\mathbf{O}_k^q$ do not include the operator-equivalent coefficients or the radial factors $\langle r^k\rangle$. Both factors are included in the parameters B_k^q, which restricts application of the B_k^q's to a single $\mathbf{J}$ manifold. The coefficients B_k^q are transformed into another set of parameters $A_k^q\langle r^k\rangle$ using the formula

$$B_k^q = A_k^q\langle r^k\rangle\langle J\|\alpha_k\|J\rangle$$

where the last factors are the operator-equivalent coefficients relating the angular momentum operators to the potential operators. The operator-equivalent coefficients are dependent on the paramagnetic center and assumed coupling scheme (e.g., **L**−**S** or intermediate). The complete set of operator-equivalent coefficients for all lanthanide ions in the **L**−**S** scheme has been presented elsewhere.[19]

The Hamiltonian H_0 is diagonalized with an arbitrary choice of a set of B_k^q coefficients and a finite external field. The determination of a complete set of eigenvalues and eigenfunctions enables the calculation of the magnetic molar susceptibility together with the isothermal magnetization using the van Vleck formalism:

$$\chi = \frac{N}{3kTZ_0}\sum_{n,i}\left[\sum_j \left|\langle\varphi_{n,i}|\mu|\varphi_{n,j}\rangle\right|^2 - 2\sum_{j,m\neq n}\frac{|\langle\varphi_{n,i}|\mu|\varphi_{m,j}\rangle|^2}{E_n - E_m}kT\right]\exp\left(-\frac{E_n}{kT}\right)$$

$$\mathbf{M} = \frac{N}{Z_H}\sum_k\langle\psi_k|\mu|\psi_k\rangle\exp\left(-\frac{E_k(\mathbf{H})}{kT}\right)$$

where $Z_0 = \sum_n d_n \exp(-E_n/kT)$ and $Z_H = \sum_k \exp(-E_k(\mathbf{H})/kT)$. The $\varphi_{n,i}$ factors denote the d_n-fold degenerate eigenfunctions with energy E_n in the absence of a magnetic field, whereas the eigensystem $\{\psi_k, E_k(\mathbf{H})\}$ was calculated with the assumption of a nonzero external magnetic field $\mathbf{H}$.

Fitting was carried out with a specially designed procedure prepared within the *Mathematica5.0* environment. The calculations were performed only with different small trial sets of two to three LF parameters. Then, the best set was chosen. The trial sets are selected on the basis of those corresponding to the distorted TTP geometry (C_3) expected for CN = 9 in **1**−**8** and the SAPR geometry (D_{4d}) expected for CN = 8 in **9**−**12**. Exceptionally, to reproduce accurately the single-crystal data for **10**, the trial sets assuming the lowest symmetry (C_1) were prepared. Such a treatment is justified if one looks at the resulting parameter sets as the effective ones. They determine the initial stage for a more systematic and extended treatment of the LF parameters in the presented compounds. More importantly, they yield initial guesses for the second stage where the magnetic coupling can be estimated.

Only for compound **12** is the first stage the final one. The remaining compounds require the introduction of magnetic interaction between the adjacent Ln^{III} and W^{V} centers. For CN = 8, the isotropic Heisenberg coupling was assumed and the term

$$H_c = -J\mathbf{S}_W\cdot\mathbf{J}$$

was added to the Hamiltonian H_0, with J denoting the coupling constant. The fitting procedure was repeated with the initial guess of the previous stage, which closes the proceedings.

In order to include in the calculations the interactions between the neighboring Ln^{III} and W^{V} paramagnetic centers coupled along the chains, the following approach was developed. The total magnetic susceptibility and the total magnetization were approximated as a sum of two separate though not independent components:

$$\chi_{total} \approx \chi_0 + \chi_c$$

$$\mathbf{M}_{total} \approx M_0 + M_c$$

where χ_0 and M_0 correspond to the values obtained in the first stage, whereas χ_c and M_c denote the corresponding corrections. The correcting terms were calculated on the basis of the following model Hamiltonian:

---

(16) Pełka, R.; Bałanda, M.; Przychodzeń, P.; Tomala, K.; Sieklucka, B.; Wasiutyński, T. *Phys. Status Solidi C* **2006**, *3*, 216.
(17) Stevens, K. W. H. *Proc. Phys. Soc., London, Sect. A* **1952**, *65*, 209.
(18) Abragam, A.; Bleaney, B. *Electron Paramagnetic Resonance of Transition Ions*; Clarendon Press: Oxford, U.K., 1970.
(19) Altshuler, S.; Kozyrev, B. M. *Electron Paramagnetic Resonance in Compounds of Transition Elements*; Nauka: Moscow, 1972.

$$H_c = \sum_{i=1}^{N} [-J_{\mathrm{eff}}\mathbf{S}_{\mathrm{D},i}\cdot(\mathbf{S}_{\mathrm{W},i} + \mathbf{S}_{\mathrm{W},i+1}) + g_{\mathrm{W}}\mathbf{S}_{\mathrm{W},i}\cdot\mathbf{H} + g_{\mathrm{eff}}\mathbf{S}_{\mathrm{D},i}\cdot\mathbf{H}]$$

by coupling the lowest-energy doublets of substates obtained in the first stage for the $\mathrm{Ln^{III}}$ centers with the adjacent spins of $\mathrm{W^V}$. The $\mathbf{S}_\mathrm{D}$ operator is the half spin operator representing effectively the magnetic features of doublets, and J_{eff} and g_{eff} denote the effective coupling constant and the effective Landé factor of the doublet, respectively. The effective quantities are related to the coupling constant J and the mean Landé factor $\bar{g}_{\mathrm{Ln}} = \mathrm{Tr}(\mathbf{g}_{\mathrm{Ln}})/3$ as follows:

$$J_{\mathrm{eff}} = J\sqrt{M_{\min}(M_{\min} + 1)}$$

$$g_{\mathrm{eff}} = \bar{g}_{\mathrm{Ln}}\sqrt{M_{\min}(M_{\min} + 1)}$$

where $M_{\min}$ is equal to the absolute value of the J_z eigenvalues corresponding to the doublet. Finally, to obtain the values of χ_c and M_c, the decoupling-limit ($J_{\mathrm{eff}} = 0$) contributions are subtracted from the calculated values of χ and M. During the second stage, the first-stage values of the LF parameters were also relaxed.

Magnetic Properties of 1. Figure 8 shows the plot of χT vs T for the powder sample of **1** (open squares). At room temperature, the χT product is equal to 1.07 $\mathrm{cm^3\ K\ mol^{-1}}$, which is slightly lower than 1.18 $\mathrm{cm^3\ K\ mol^{-1}}$, corresponding to the isolated $\mathrm{Ce^{III}}$ ($\mathbf{J} = {}^5/_2$, $g_J = {}^6/_7$) and $\mathrm{W^V}$ ($S = {}^1/_2$, $g = 2$) ions. As the temperature is lowered, the χT product gradually decreases to reach a short plateau of 0.84 $\mathrm{cm^3\ K\ mol^{-1}}$ and then abruptly decreases to the value of 0.58 $\mathrm{cm^3\ K\ mol^{-1}}$ at $T = 2$ K. In the inset to Figure 8, the experimental data for the field dependence of the magnetization at $T = 2$ K are shown (open circles). The corresponding curve displays a monotonic increase with increasing value of the magnetic field and reaches the value of 1.47 $N\beta$ at $H = 50$ kOe. It is twice lower than the value of 2.81 $N\beta$ expected for the isolated $\mathrm{Ce^{III}}$ and $\mathrm{W^V}$ ions.

Figure 8 shows the best fits (solid lines) for χT vs T and M vs H data obtained with the set of parameters presented in Table 10. The lowest sublevel is a Kramers doublet comprising $|\pm{}^5/_2\rangle$ states (Table 11); hence, $M_{\min} = {}^5/_2$. The lowest substates are those with the highest $|\mathbf{J}_z|$ value within the $\mathbf{J} = {}^5/_2$ ground-state multiplet. This indicates the appearance of strong uniaxial magnetic anisotropy along the C_4 axis at low temperatures. The sudden drop of χT at low temperatures may be ascribed to two factors. First and the dominating one is the “switching-on” of the intrachain antiferromagnetic interaction. The second is related to the rapid depopulation of the first excited-state level in favor of the ground state, from 24% at $T = 10$ K down to 0.3% at $T = 2$ K. The slow increase of the χT values starting from about 10 K and continuing up to room temperature is, in turn, consistent with the position of the highest excited-state level ($|\pm{}^3/_2\rangle$ states) on the energy scale high above (≈230 $\mathrm{cm^{-1}}$) the ground state.

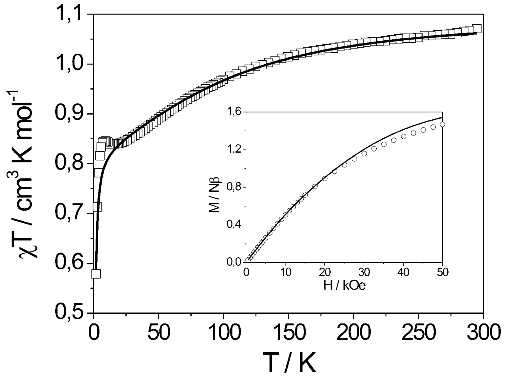

Figure 8. Thermal dependence of χT for **1** with the best fit (solid line). Inset: M vs H with the best fit (solid line).

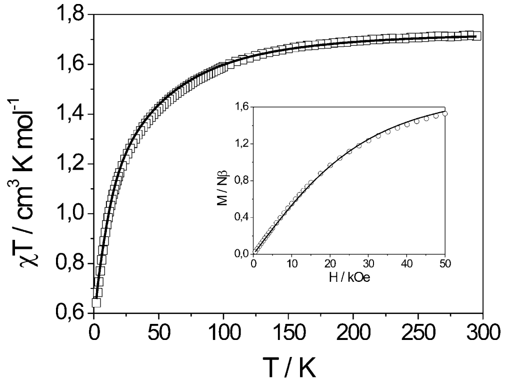

Figure 9. Thermal dependence of χT for **2** with the best fit (solid line). Inset: M vs H with the best fit (solid line).

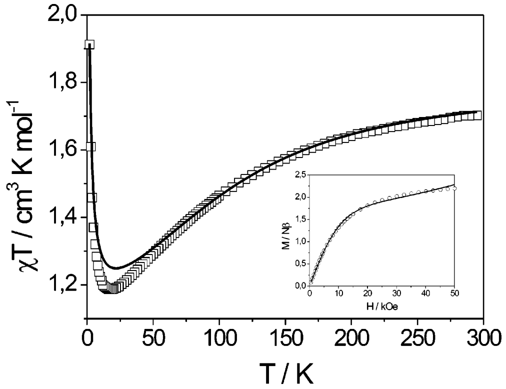

Figure 10. Thermal dependence of χT for **3** with the best fit (solid line). Inset: M vs H with the best fit (solid line).

Magnetic Properties of 2. In Figure 9, the plot of χT vs T for the powder sample of **2** is shown (open squares). The corresponding curve displays a smooth monotonic increase with increasing temperature starting at the value of 0.64 $\mathrm{cm^3\ K\ mol^{-1}}$ for $T = 2$ K to reach the value of 1.71 $\mathrm{cm^3\ K\ mol^{-1}}$ at room temperature, which is lower than 1.98 $\mathrm{cm^3\ K\ mol^{-1}}$ expected for the isolated $\mathrm{Pr^{III}}$ ($\mathbf{J} = 4$, $g_J = {}^4/_5$) and $\mathrm{W^V}$ ($S = {}^1/_2$, $g = 2$) ions. The inset to Figure 9 shows the plot of isothermal magnetization M vs external magnetic field H for at $T = 2$ K (open circles). The monotonically increasing magnetization curve reaches the value of 1.53 $N\beta$ at $H = 50$ kOe. It is considerably lower than the value of 3.85 $N\beta$ expected for the noninteracting ions approximation.

Figure 9 shows the best-fit curves (solid lines) for χT vs T and M vs H data simulated with the parameters presented in Table 10. The lowest level of the ground-state multiplet is the doublet of $|\pm 2\rangle$ substates (Table 12); thus, $M_{\min} = 2$. At $T = 2$ K, the population of the ground-state level is almost

Table 10. Best-Fit Parameters for Compounds **1**−**4** and **6**−**11**

compound	ground-state term	g_{Ln}	J/cm^{-1}	$A_2^0\langle r^2\rangle$/cm^{-1}	$A_4^0\langle r^4\rangle$/cm^{-1}	$A_6^0\langle r^6\rangle$/cm^{-1}	$A_6^4\langle r^6\rangle$/cm^{-1}
1	$^2F_{5/2}$	0.81(2)	−0.24(1)	+55(2)	−127(6)		
2	$^3H_4$	0.74(3)	−0.07(3)	−94(11)	−30(3)		
3	$^4I_{9/2}$	0.67(1)	+0.47(2)		+45(2)	−86(4)	
4	$^6H_{5/2}$	0.13(3)	+1.25(3)				
6	$^8S_{7/2}$	1.97(2)	−1.44(3)				
7	$^7F_6$	1.47(2)	+0.28(7)	+81(1)	+51(6)		
8	$^6H_{15/2}$	1.28(3)	+0.23(1)	+164(22)	−105(12)		
9	$^5I_8$	1.24(1)	−0.04(1)	+300(6)	−177(10)	+6(1)	−483(53)
10	$^4I_{15/2}$	1.18(2)	+0.06(1)				
11	$^2F_{7/2}$	1.15(5)	−0.07(2)	+5.5(3)		+147(11)	−244(23)

Table 11. Energies and Wave Functions of the Ground-State Multiplets for Ce^{III}

E_n (cm^{-1})	wave function	E_n (cm^{-1})	wave function
0	$\|^5/_2\rangle, \|-^5/_2\rangle$	231	$\|^3/_2\rangle, \|-^3/_2\rangle$
8	$\|^1/_2\rangle, \|-^1/_2\rangle$		

Table 12. Energies and Wave Functions of the Ground-State Multiplets for Pr^{III}

E_n (cm^{-1})	wave function	E_n (cm^{-1})	wave function
0	$\|2\rangle, \|-2\rangle$	145	$\|4\rangle, \|-4\rangle$
47	$\|3\rangle, \|-3\rangle$	217	$\|0\rangle$
131	$\|1\rangle, \|-1\rangle$		

Table 13. Energies and Wave Functions of the Ground-State Multiplets for Nd^{III}

E_n (cm^{-1})	wave function	E_n (cm^{-1})	wave function
0	$\|^7/_2\rangle, \|-^7/_2\rangle$	252	$\|^3/_2\rangle, \|-^3/_2\rangle$
5	$\|^1/_2\rangle, \|-^1/_2\rangle$	340	$\|^5/_2\rangle, \|-^5/_2\rangle$
186	$\|^9/_2\rangle, \|-^9/_2\rangle$		

100%, and then it drops to 77% at $T = 50$ K, whereas the first excited-state level corresponding to the higher $|\mathbf{J}_z|$ value ($|\pm3\rangle$ states) becomes populated to 20%. At $T = 100$ K, the population of the third excited-state level corresponding to the highest $|J_z|$ substates amounts to 7%. Those facts explain the relatively rapid increase of the χT product in the low-temperature range. At higher temperatures, compound **2** is isotropic down to about 150 K, which is the region where $|\pm1\rangle$ and $|\pm4\rangle$ states become depopulated, whereas the $|\pm2\rangle$ and $|\pm3\rangle$ states' population starts to prevail.

Magnetic Properties of 3. Figure 10 shows the plot of χT vs T for the powder sample of **3** (open squares). As the temperature rises, the χT product gradually increases, reaching the value of 1.70 cm^3 K mol^{-1} at $T = 300$ K, which is lower than 2.01 cm^3 K mol^{-1} corresponding to the noninteracting Nd^{III} ($\mathbf{J} = {}^9/_2$, $g_J = {}^8/_{11}$) and W^V ($S = {}^1/_2$, $g = 2$) ions. At $T = 18$ K, the χT product displays a minimum of 1.19 cm^3 K mol^{-1} and then increases abruptly, reaching the value of 1.91 cm^3 K mol^{-1} at $T = 2$ K. The inset to Figure 10 presents the experimental data for the field dependence of the magnetization at $T = 2$ K (open circles). The corresponding curve displays a monotonic increase, nearly saturating the highest fields. It reaches the value of 2.20 $N\beta$ at $H = 50$ kOe, which is lower than 3.90 $N\beta$ expected for the isolated-ion approximation.

Figure 10 presents the best-fit curves (solid lines) for χT vs T and M vs H data obtained for the parameters listed in Table 10. The lowest sublevel for the isolated Nd^{III} is a Kramers doublet comprising $|\pm^7/_2\rangle$ states (Table 13), which implies $M_{min} = {}^7/_2$. These states correspond to the second largest $|\mathbf{J}_z|$ value within the ground-state multiplet. Nevertheless, the strong uniaxial magnetic anisotropy should be set only at very low temperatures because of the first excited-state level lying at 5 cm^{-1} and comprising $|\pm^1/_2\rangle$ states. The next excited-state Kramers doublet ($|\pm^9/_2\rangle$) lying about 190 cm^{-1} above the ground state and the low-lying first excited-state level are accountable for the relatively slow increase of the χT values starting from 20 K. The population of the second excited-state level stops being negligible only at $T = 100$ K (3%). The population of the $|\pm^7/_2\rangle$ level reaches 97% at $T = 2$ K, whereas that to the $|\pm^1/_2\rangle$ level is 3%. At $T = 10$ K, they repopulate to the amounts 67% and 33%, respectively. The proximity of the $|\pm^1/_2\rangle$ level to the ground state confines the range of the applicability of the present approximate approach to very low temperatures. However, the coupling constant was found to be only a fraction of a wavenumber, so that intrachain interactions are practically "switched off" at about 10 K, where the population of the ground state still dominates and the approach remains plausible. Moreover, coupling with the first excited-state doublet is expected to be weaker than that with the ground state. More importantly, this does not discredit the main point of the analysis; i.e., coupling between the lowest substate(s) of Ln^{III} and the states of the W^V ion is sufficient to determine the magnetic characteristics of lanthanide-based systems at low temperatures because of the LF splitting from the full ground-state multiplet of Ln^{III}. The ferromagnetic coupling between the doublet ground state of Nd^{III} and the doublet of W^V is accountable for the rapid increase of χT observed below 10 K.

Magnetic Properties of 4. The experimental thermal dependence of the χT product for **4** in the range of 2−300 K is shown in Figure 11 (triangles). Upon cooling, χT continuously decreases to reach a minimum at $T = 15$ K. Further cooling provides a sharp increase, and the value of 0.791 cm^3 K mol^{-1} at $T = 2$ K is reached. The ^6H ground-state term of the Sm^{III} ion is known to be split by the spin−orbit coupling into six levels: $E(\mathbf{J}) = \lambda\mathbf{J}(\mathbf{J} + 1)/2$ with the spin−orbit coupling parameter λ on the order of 200 cm^{-1} and $\mathbf{J} = {}^5/_2, ..., {}^{15}/_2$.[15] Therefore, in addition to the ground state $^6H_{5/2}$, the first ($^6H_{7/2}$) and even higher excited states can be considerably populated at room temperature. As a consequence, the high-temperature behavior of χT vs T deviates from linearity. Furthermore, the presence of low-lying excited states adds a significant temperature-independent contribution to the magnetic susceptibility. To take both

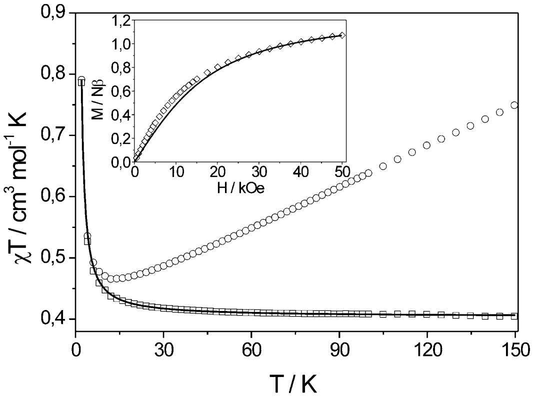

Figure 11. Thermal dependence of χT for **4** with the best fit (solid line). Inset: M vs H with the best fit (solid line).

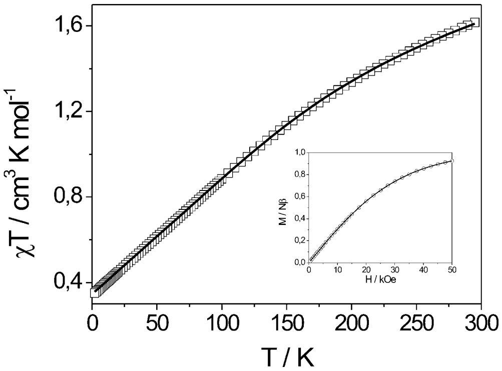

Figure 12. Thermal dependence of χT for **5** with the best fit (solid line). Inset: M vs H with the best fit (solid line).

effects into account, the stepwise fitting procedure was applied. First, it involved subtraction of a nonlinear (temperature-dependent) contribution from the experimental data. The second step consisted of fitting of the Curie−Weiss law and temperature-independent correction χ^*. The best fit was obtained with $\lambda = 212$ cm^{-1}, $C = 0.404$ cm^3 K mol^{-1}, $\theta = +0.97$ K, and $\chi^* = 0.0022$ cm^3 mol^{-1}. The high value of χ^* is probably due to the splitting of the ^{6}H ground state of the Sm$^{\text{III}}$ ion (LF effects). The data corrected with χ^* (Figure 11, circles) have provided the starting point for further analysis, revealing the best fit for **4** with $J = +1.25(3)$ cm^{-1} and $g_{\text{Sm}} = 0.13(3)$ (Figure 11, solid lines). The isothermal magnetization curve for **4** at $T = 2$ K (Figure 11, inset) shows a small difference between simulated and experimental data in the low applied field, which is attributable to the neglected interchain interaction.

Magnetic Properties of 5. The experimental thermal dependence of the χT product for **5** in the range of 2−300 K is shown in Figure 12. At room temperature, the value of χT is equal to 1.62 cm^3 K mol^{-1}, which is greater than the value expected for the sole contribution from the W$^{\text{V}}$ ion ($S = {}^1/_2$, $g = 2$) and significantly lower than the high-temperature limit (7.88 cm^3 K mol^{-1}) corresponding to the decoupled total spin **S** and the total orbital angular momentum **L** of the Eu$^{\text{III}}$ ion. Upon cooling, χT monotonically decreases along a smooth and featureless curve to reach the value of 0.35 cm^3 K mol^{-1} at $T = 2$ K.

The ^{7}F ground-state term of the Eu$^{\text{III}}$ ion is split by the spin−orbit coupling into seven states ^{7}F$_J$, with J taking the integer values from 0 to 6. The spin−orbit coupling operator with a λ spin−orbit coupling parameter can be expressed as $\mathbf{H}_{\text{SO}} = \lambda\mathbf{L}\cdot\mathbf{S}$. The ^{7}F$_0$ ground state is taken as the origin in the $E(\mathbf{J}) = \lambda\mathbf{J}(\mathbf{J} + 1)/2$ energy scheme. Despite the ground state being diamagnetic, the nonzero contribution to magnetic susceptibility has been taken into account because of the low-lying first excited states, which can be thermally populated.[15] The molar magnetic susceptibility can be expressed as

$$\chi_{\text{Eu}} = \frac{\sum_{J=0}^{6}(2J + 1)\chi(J)\exp[-\lambda J(J + 1)/2k_{\text{B}}T]}{\sum_{J=0}^{6}(2J + 1)\exp[-\lambda J(J + 1)/2k_{\text{B}}T]}$$

where

$$\chi(J) = \frac{Ng_J{}^2\beta^2 J(J + 1)}{3kT} + \frac{2N\beta^2(g_J - 1)(g_J - 2)}{3\lambda}$$

The first term in the above formula is the standard contribution from a noninteracting magnetic center with spin quantum number J and Landé factor gJ ($g_J = {}^3/_2$ for $\mathbf{J} \neq 0$ and $g_J = 5$ for $\mathbf{J} = 0$), whereas the other one represents a temperature-independent contribution due to the presence of low-lying excited states. This contribution is a second-order quantum correction calculated as

$$\tilde{\chi} = -2N\sum_{M_J=-J}^{+J}\sum_{J'\neq J}\sum_{M_{J'}=-J'}^{+J'}\frac{\langle J,M_J|\beta(\mathbf{L} + 2\mathbf{S})|J',M_{J'}\rangle}{E(J,M_J) - E(J',M_{J'})}$$

The neglect of magnetic coupling with the adjacent W$^{\text{V}}$ ions and independent treatment of both centers can be assumed with a good approximation because the ground state of the Eu$^{\text{III}}$ ion is diamagnetic. The contribution to the molar magnetic susceptibility from the W$^{\text{V}}$ center is calculated as

$$\chi_{\text{W}} = \frac{Ng_{\text{W}}{}^2\beta^2 S(S + 1)}{3kT}$$

where g_{W} is the Landé factor of the W$^{\text{V}}$ ion. The total magnetic susceptibility calculated as a sum $\chi_{\text{total}} = \chi_{\text{Eu}} + \chi_{\text{W}}$ has been implemented in the fitting procedure. The best fit was obtained for $g_{\text{W}} = 1.92(2)$ and $\lambda = 386(4)$ cm^{-1} with $g_{J=0}$ fixed at 5 and $g_{J\neq 0}$ at $^3/_2$. Figure 12 shows the magnetic molar susceptibility in the form of a χT vs T experimental curve (open squares) together with the simulated curve (solid line). The inset to Figure 12 shows the magnetization M vs external magnetic field H measured at $T = 2$ K (open circles). The solid curve corresponds to the sole contribution from the noninteracting W$^{\text{V}}$ center given by the following formula:

$$M = \frac{1}{2}Ng_{\text{W}}\beta\tanh\left(\frac{g_{\text{W}}\beta H}{2kT}\right)$$

The theoretical analysis performed for **5** clearly shows that the Eu$^{\text{III}}$ and W$^{\text{V}}$ centers in 1-D chains are magnetically decoupled.

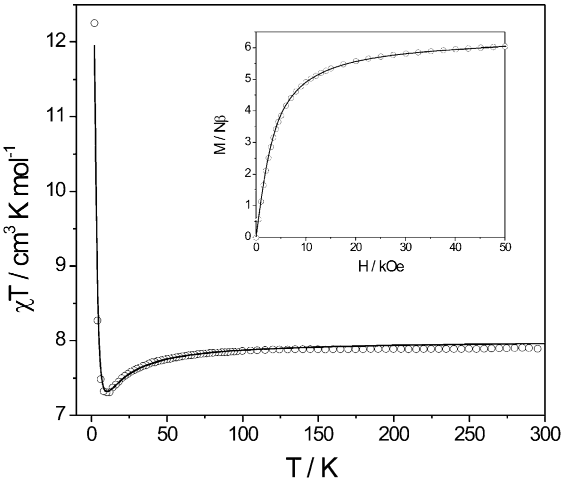

Figure 13. Thermal dependence of χT for **6** with the best fit (solid line). Inset: M vs H with the best fit (solid line).

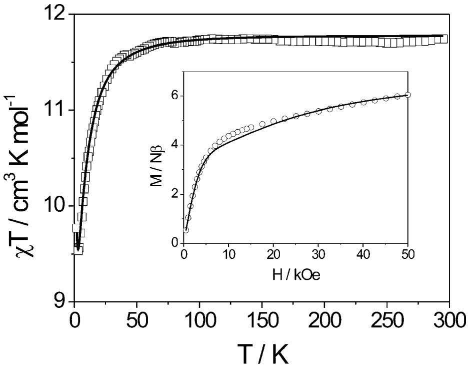

Figure 14. Thermal dependence of χT for **7** with the best fit (solid line). Inset: M vs H with the best fit (solid line).

Magnetic Properties of 6. Figure 13 shows the plot of χT vs T for a powder sample of **6** measured in the temperature range 2−300 K at a direct current field of 1 kOe. At room temperature, χT is equal to 7.9 cm^3 K mol^{-1}, which is slightly lower than 8.25 cm^3 K mol^{-1} expected for an isolated Gd^{III} ion ($S = {}^7/_2$ with ground state $^8S_{7/2}$) and a W^V ion ($S = {}^1/_2$) with $g = 2.00$. Below 100 K, the χT product decreases to reach the minimum at 11 K. Upon further cooling, a sharp increase is observed, and the value of 12.25 cm^3 K mol^{-1} at $T = 2$ K is reached. The χT vs T obeys the Curie−Weiss law above 12 K with $C = 7.94$ cm^3 K mol^{-1} and $\theta = -1.14$ K. The data for **6** were well simulated down to 2 K with $J = -1.44(3)$ cm^{-1} and $g_{Gd} = 1.97(2)$ (Figure 13, solid lines).

Magnetic Properties of 7. Figure 14 shows the plot of χT vs T for a powder sample of **7** (open squares). In a wide range of temperature, the corresponding curve displays an almost plateau behavior with only slight deviations from the value of 11.74 cm^3 K mol^{-1} reached at room temperature, which is lower than 12.19 cm^3 K mol^{-1} expected for the isolated Tb^{III} ($\mathbf{J} = 6$, $g_J = {}^3/_2$) and W^V ($S = {}^1/_2$, $g = 2$) ions. Below $T \approx 25$ K, the χT product gradually decreases, showing a slight upturn for the lowest temperatures, with the value of 9.77 cm^3 K mol^{-1} reached at $T = 2$ K. In the inset to Figure 14, the isothermal magnetization M vs external magnetic field H plot for **7** measured at $T = 2$ K (open circles) is shown. The magnetization curve displays a relatively rapid increase up to $H \approx 10$ kOe and then embarks on a nearly linear rise, reaching the value of 6.05 $N\beta$ at $H = 50$ kOe. This value is considerably lower than 9.80 $N\beta$ calculated within the noninteracting ions approximation.

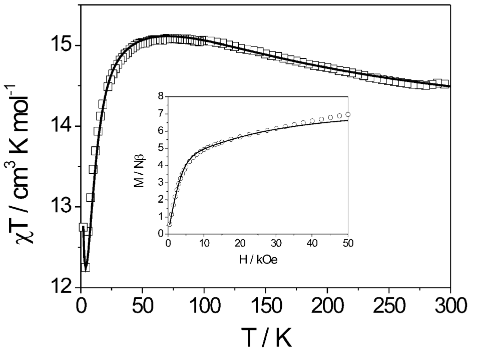

Figure 15. Thermal dependence of χT for **8** with the best fit (solid line). Inset: M vs H with the best fit (solid line).

Table 14. Energies and Wave Functions of the Ground-State Multiplets for Tb^{III}

E_n (cm^{-1})	wave function	E_n (cm^{-1})	wave function
0	$\|5\rangle, \|-5\rangle$	81	$\|2\rangle, \|-2\rangle$
11	$\|4\rangle, \|-4\rangle$	108	$\|1\rangle, \|-1\rangle$
35	$\|6\rangle, \|-6\rangle$	118	$\|0\rangle$
44	$\|3\rangle, \|-3\rangle$		

Figure 14 shows the best-fit curves (solid lines) for χT vs T and M vs H data simulated with the set of parameters collected in Table 10. The lowest substate of the ground-state multiplet of the Tb^{III} ion is a doublet of $|\pm 5\rangle$ states (Table 14); hence, $M_{min} = 5$. The first excited substates $|\pm 4\rangle$ lie at about 10 cm^{-1}. At $T = 2$ K, the population of the ground-state level is greater than 99%, and then at $T = 20$ K, it drops to 63%, while that of the $|\pm 4\rangle$ level amounts to 29%. The relatively rapid change in the χT value in the low-temperature range may be ascribed to the rapid increase of the population of the $|\pm 4\rangle$ level. The highest energy level corresponds to the nondegenerate $|0\rangle$ state and lies at about 118 cm^{-1}. The following levels correspond to the subsequent low $|J_z|$ values down to the point of 40 cm^{-1}, below which the high $|\mathbf{J}_z|$ states reside. This may explain the nearly plateaulike behavior of χT persisting down to 50 K. Furthermore, the small upturn of the χT product at lowest temperatures indicates ferromagnetic coupling between W^V and Tb^{III} spin states.

Magnetic Properties of 8. In Figure 15, the plot of χT product vs T for a powder sample of **8** (open squares) is presented. At room temperature, the χT product is equal to 14.52 cm^3 K mol^{-1}, which corresponds to the χT value calculated for the isolated Dy^{III} ($\mathbf{J} = {}^{15}/_2$, $g_J = {}^4/_3$) and W^V ($S = {}^1/_2$, $g = 2$) centers. As the temperature is lowered, the χT product gradually increases to reach at $T \approx 72$ K a dispersed maximum of 15.08 cm^3 K cm^{-1} and then abruptly decreases to the value of 12.75 cm^3 K mol^{-1}, reached at $T = 2$ K. The inset to Figure 15 shows the plot of the isothermal magnetization M vs external magnetic field H for **8** measured at $T = 2$ K (open circles). The shape of the magnetization curve is similar to that for **7**. The magnetiza-

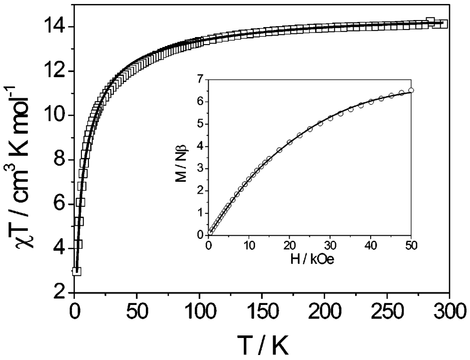

Figure 16. Thermal dependence of χT for [HoW] (**9**) with the best fit (solid line). Inset: M vs H with the best fit (solid line).

Table 15. Energies and Wave Functions of the Ground-State Multiplets for $\mathrm{Dy^{III}}$

E_n (cm^{-1})	wave function	E_n (cm^{-1})	wave function
0	$\lvert {}^{11}/_2\rangle, \lvert -{}^{11}/_2\rangle$	104	$\lvert {}^{15}/_2\rangle, \lvert -{}^{15}/_2\rangle$
11	$\lvert {}^{13}/_2\rangle, \lvert -{}^{13}/_2\rangle$	167	$\lvert {}^{5}/_2\rangle, \lvert -{}^{5}/_2\rangle$
39	$\lvert {}^{9}/_2\rangle, \lvert -{}^{9}/_2\rangle$	219	$\lvert {}^{3}/_2\rangle, \lvert -{}^{3}/_2\rangle$
101	$\lvert {}^{7}/_2\rangle, \lvert -{}^{7}/_2\rangle$	248	$\lvert {}^{1}/_2\rangle, \lvert -{}^{1}/_2\rangle$

tion curve displays a relatively rapid increase up to $H \approx 10$ kOe and then embarks on a nearly linear rise, reaching the value of 6.97 $N\beta$, which is considerably lower than 10.77 $N\beta$ calculated within the noninteracting ions approximation.

Figure 15 shows the best-fit curves (solid lines) for χT vs T and M vs H data obtained with the parameters presented in Table 10. The lowest level of the ground-state multiplet is the Kramers doublet of $\lvert \pm {}^{11}/_2\rangle$ substates (Table 15); thus, $M_{\mathrm{min}} = {}^{11}/_2$. The next substates $\lvert \pm {}^{13}/_2\rangle$ lie about 10 cm^{-1} above. At $T = 2$ K, the population of the ground-state level is greater than 99%, and then at $T = 20$ K, it drops to 66%, while that of the $\lvert \pm {}^{13}/_2\rangle$ level amounts to 30%. The relatively rapid change in the χT value in the low-temperature range may be ascribed to that rapid increase of the population of the $\lvert \pm {}^{13}/_2\rangle$ level. The dispersed maximum displayed around 70 K may be understood as a combined effect of the anisotropy of the g_{Dy} tensor and the LF reordering of the $\mathrm{Dy^{III}}$ multiplet components so that the substates with the highest $\lvert \mathbf{J}_z\rvert$ values are pushed toward lower energies.

Magnetic Properties of 9. Figure 16 shows the plot of the χT product vs temperature T for a powder sample of [HoW] (**9**) (open squares). As temperature rises, χT asymptotically approaches the value of 14.44 cm^3 K mol^{-1}, corresponding to the contributions from isolated $\mathrm{Ho^{III}}$ ($\mathbf{J} = 8$, $g = {}^5/_4$) and $\mathrm{W^V}$ ($S = {}^1/_2$, $g = 2$) ions. When the temperature is lowered, the χT product gradually decreases to reach the value of 2.96 cm^3 K mol^{-1} at $T = 2$ K. In the inset to Figure 16, the experimental data for the field dependence of the magnetization at $T = 2$ K are shown (open circles). The corresponding curve displays a monotonic increase with the increasing value of the magnetic field and reaches the value of 6.53 $N\beta$ at $H = 50$ kOe, which is significantly lower than the value of 10.76 $N\beta$ expected for the isolated $\mathrm{Ho^{III}}$ and $\mathrm{W^V}$ centers.

Figure 16 shows the best-fit curves (solid lines) for the susceptibility and isothermal magnetization obtained with the parameters listed in Table 10. The lowest substate of the ground-state multiplet is a superposition of $\{\lvert 6\rangle + \lvert -6\rangle\}$ and $\{\lvert 2\rangle + \lvert -2\rangle\}$ states (see Table S2 in the Supporting Information). The wave functions of [HoW] collected in Table S3 in the Supporting Information are expressed as superpositions of those given in Table S2 in the Supporting Information and the $\mathrm{W^V}$ spin wave functions. The introduction of the Heisenberg coupling between the $\mathrm{Ho^{III}}$ and $\mathrm{W^V}$ centers splits and shifts the levels slightly, but the spectrum can be seen to consist of the Kramers doublets. The first excited state of **9** lies as close as 7.3 cm^{-1} to the ground-state level, and the separation between the subsequent excited states is on the order of tens of reciprocal centimeters, so that the entire spectrum is taken into account in the calculation of the magnetic properties of **9**.

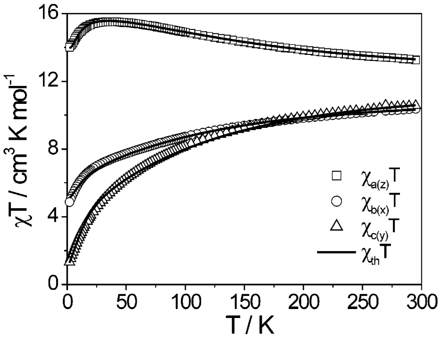

Figure 17. Thermal dependence of χT measured on a single crystal of [ErW] (**10**) with the best fit (solid lines).

Magnetic Properties of 10. The magnetic measurements for [ErW] (**10**) were performed on a single crystal having a size of 4.7 × 0.8 × 0.6 mm^3. The orientation of the axes was determined by the X-ray analysis. Figure 17 shows the experimental temperature dependence of the χT product in an external magnetic field of 1 kOe applied in three independent directions along the a (open squares), b (open circles), and c (open triangles) crystal axes. Even at 300 K, the susceptibility measured along the a crystal direction is separated from those measured along the b and c directions. The value of 11.85 cm^3 K mol^{-1} expected for the noninteracting $\mathrm{Er^{III}}$ ($\mathbf{J} = {}^{15}/_2$, $g = {}^6/_5$) and $\mathrm{W^V}$ ($S = {}^1/_2$, $g = 2$) ions lies between the high-temperature values of χT for $H \| a$ and those for $H \| b$ or $H \| c$. The χT values for both $H \| b$ and $H \| c$ smoothly decrease when the temperature is lowered. The corresponding curves coincide for high temperatures and separate at $T \approx 150$ K, with the decrease of the $H \| c$ data being more rapid. The χT product for $H \| a$ displays a steady increase upon cooling, reaching the maximum of 15.52 cm^3 K mol^{-1} at $T = 38$ K, and then decreases, amounting to 14.01 cm^3 K mol^{-1} at $T = 2$ K, showing a slight upturn for the lowest temperatures. The experimental data reveal that [ErW] is a uniaxial magnet at high temperatures, with the a direction playing the role of an easy axis. Below $T \approx 150$ K, the sample becomes magnetically biaxial. However, the a axis continues to define the preferred direction of magnetization down to the lowest temperatures. Figure 18 shows the field dependence of the magnetization at $T = 2$ K measured along three crystallographic directions. The magnitude and the rate of change of magnetization are consistent with the corresponding values of χT detected at 2 K.

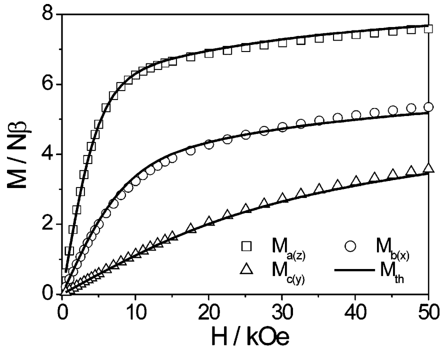

Figure 18. Field dependence of magnetization measured on a single crystal of [ErW] (**10**) with the best fit (solid line).

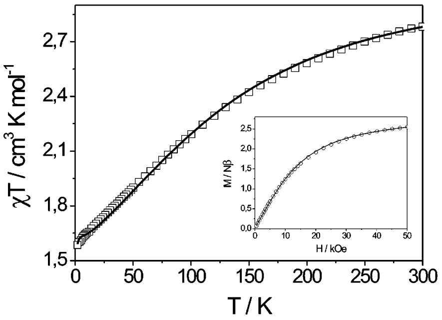

Figure 19. Thermal dependence of χT for [YbW] (**11**) with the best fit (solid line). Inset: M vs H with the best fit (solid line).

Table 16. LF Parameters (cm^{-1}) for Er^{III}

	LF parameter		LF parameter
$A_2^0\langle r^2\rangle$	$-200(8)$	$A'^2_6\langle r^6\rangle$	$+396(13)$
$A_2^1\langle r^2\rangle$	$+1040(140)$	$A_6^3\langle r^6\rangle$	$-168(34)$
$A_4^0\langle r^4\rangle$	$+16(3)$	$A_6^4\langle r^6\rangle$	$+359(7)$
$A_4^3\langle r^4\rangle$	$-282(47)$	$A'^4_6\langle r^6\rangle$	$-77(13)$
$A_6^0\langle r^6\rangle$	$-5(1)$		

The best-fit curves (solid lines) of the susceptibility and isothermal magnetization for the three indicated directions shown in Figures 17 and 18, respectively, were simulated with the set of parameters collected in Table 10 and the LF parameters listed in Table 16. The primed LF parameters are also given because of the low symmetry of the Er^{III} coordination environment. The lowest level of the ground-state multiplet is a Kramers doublet with the largest contributions from the highest spin states $|\pm^{11}/_2\rangle$, $|\pm^{15}/_2\rangle$, and $|\pm^{13}/_2\rangle$ (Table S4 in the Supporting Information). The wave functions of **10** presented in Table S5 in the Supporting Information are expressed as superpositions of those given in Table S4 in the Supporting Information and the W^V spin wave functions. The first excited state of **10** lies less than 0.1 cm^{-1} above the ground state, and the separation between the two following excited states is on the order of wavenumber fractions only. The degeneracy in the spectrum of **10** is completely removed. In the calculation of the magnetic properties, the whole spectrum is taken into account.

Magnetic Properties of 11. Figure 19 shows the plot of χT vs T for a powder sample of [YbW] (**11**) (open squares). As the temperature decreases, χT gradually decreases from the value of 2.78 cm^3 K mol^{-1} at $T = 300$ K, which is lower than 2.95 cm^3 K mol^{-1} corresponding to the isolated-ion contributions from the W^V ($S = ^1/_2$, $g = 2$) and Yb^{III} ($\mathbf{J} = ^7/_2$, $g = ^8/_7$) centers. At $T = 2$ K, the χT product attains the value of 1.58 cm^3 K mol^{-1}. In the inset to Figure 19, the experimental data for the field dependence of isothermal magnetization at $T = 2$ K are shown (open circles). The corresponding curve displays a monotonic increase with increasing value of the magnetic field and reaches the value of 2.54 $N\beta$ at $H = 50$ kOe. It is significantly lower than the value of 4.74 $N\beta$ expected for the isolated-ion approximation calculated at the same temperature and external magnetic field.

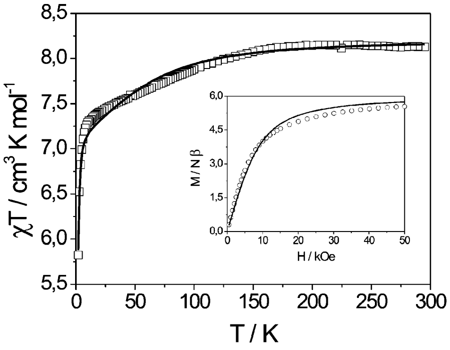

Figure 20. Thermal dependence of χT for [TmW] (**12**) with the best fit (solid line). Inset: M vs H with the best fit (solid line).

Figure 19 shows the best-fit curves (solid lines) for the susceptibility and isothermal magnetization obtained with the parameters given in Table 10. The lowest substate of the ground-state multiplet is a superposition of $|\pm^1/_2\rangle$ and $|\pm^7/_2\rangle$ states (Table S6 in the Supporting Information) in which the lowest spin-state contribution is dominating. That accounts for the considerable downshift of isothermal magnetization at 2 K (Figure 19). The wave functions of [YbW] (Table S7 in the Supporting Information) are expressed as superpositions of those given in Table S6 in the Supporting Information and W^V ion spin wave functions.

Magnetic Properties of 12. Figure 20 shows the plot of χT vs T for a powder sample of [TmW] (**12**) (open squares). In the range of 180−300 K, the corresponding curve displays a plateau of 8.13 cm^3 K mol^{-1}, slightly higher than 7.52 cm^3 K mol^{-1}, which comprises the contributions from the isolated Tm^{III} ($\mathbf{J} = 6$, $g = ^7/_6$) and W^V ($S = ^1/_2$, $g = 2$) centers. When the temperature is lowered below 180 K, the χT product initially decreases gently, and then upon further cooling down to 10 K, it undergoes an abrupt drop to reach the value of 5.83 cm^3 K mol^{-1} at $T = 2$ K. In Figure 20, the plot of isothermal magnetization M vs external magnetic field H for [TmW] at $T = 2$ K (open circles) is shown. The monotonically increasing magnetization curve reaches the value of 5.54 $N\beta$ at $H = 50$ kOe, which is considerably lower than the value of 7.74 $N\beta$ expected for the noninteracting ions approximation.

The $4f^{12}$ electronic configuration of the Tm^{III} ion results in the ground-state $^3H_6$ with the expected value of the Landé factor $^7/_6$. The dimension of the ground-state subspace is hence 13, whereas that of the subspace spanned by the W^V ion spin states is 2. The ions are treated independently; i.e., no magnetic coupling between them is assumed. The best fit to the experimental data was found for the following set of parameters: $g_{\mathrm{Tm}} = 1.22(2)$, $A_2^0\langle r^2\rangle = +199(10)$ cm^{-1}, $A_4^0\langle r^4\rangle = -16(2)$ cm^{-1}, and $A_4^4\langle r^4\rangle = -425(17)$ cm^{-1}. The LF obtained in the applied approximation does not remove the degeneracy of the ground-state multiplet completely. In **12**, the three lowest substates (of which one is a degenerate pair) lie within 5 cm^{-1} (Table S8 in the Supporting Information). The lowest sublevel is a superposition of $|0\rangle$ and $\{|4\rangle + |-4\rangle\}$. The magnetic behavior of **12** in the low-temperature range is determined by the three lowest sublevels because the fourth substate lies at fairly high energy (about 120 cm^{-1}). Figure 20 shows the best-fit curves (solid lines) for the susceptibility and isothermal magnetization.

Conclusions

Two series of isomorphous compounds, (i) 1-D chains [Ln(terpy)(DMF)$_4$][W(CN)$_8$]·6H$_2$O (Ln = Ce−Dy) and (ii) dinuclear molecules [Ln(terpy)(DMF)$_2$(H$_2$O)$_2$][W(CN)$_8$]·3H$_2$O (Ln = Ho, Er, Yb), along with the ionic system [Tm(terpy)(DMF)$_2$(H$_2$O)$_3$][W(CN)$_8$]·4H$_2$O·DMF, provide the foundation of magnetostructural correlation analysis. We introduced the unique method of calculation of the LF splitting parameters and the exchange interaction between lanthanide centers and a d-electron spin carrier. The corresponding exchange constants have been shown to change the sign along the series of chains. The coupling is antiferromagnetic for **1** ($J = -0.24$ cm^{-1}) and **2** ($J = -0.07$ cm^{-1}), where the latter is apparently weaker, opening the possibility for *sign flip* to occur for the subsequent lanthanide center. Indeed, the intrachain interaction observed for **3** ($J = +0.47$ cm^{-1}), **7** ($J = +0.28$ cm^{-1}), and **8** ($J = +0.23$ cm^{-1}) has ferromagnetic character. In the case of dimeric systems, the coupling constants seem to be independent of the lanthanide center. The splitting structures of the ground-state multiplets of the compounds have been shown to explain the temperature dependences of the magnetic susceptibilities. Furthermore, the information on the 4f−5d electronic structures reported here provides a good starting point for studying the magnetic anisotropies of single crystals.

The magnetic coupling between the Ln$^{\mathrm{III}}$ and W$^{\mathrm{V}}$ centers has been found to be very weak. Small values of calculated coupling constants appear as a consequence of very long Ln$^{\mathrm{III}}$−NC−W$^{\mathrm{V}}$ cyano bridges. The coupling constant values show a decreasing tendency with an increase of the number of f-shell electrons.

Acknowledgment. This work was partially supported by the JSPS fellowship No. P05736 to R.P., Committee for Scientific Research in Poland (KBN) Grant PB 1274, and NoE “MAGMANet” (Grant NMP3-CT-2005-515767). R.P. is grateful to Prof. Kazuya Saito at the University of Tsukuba for his kind hospitality.

Supporting Information Available: Table containing extended operator equivalents $\mathbf{O}_k^q$ (Table S1), tables showing energies and wave functions of the ground-state multiplets and for compounds **9**−**11** (Tables S2−S8), and crystallographic files in CIF format for compounds **1·C$_2$H$_5$OH**−**8·C$_2$H$_5$OH** and **9**−**12**. This material is available free of charge via the Internet at http://pubs.acs.org.

IC700795Q